Glutamatergic drive along the septo-temporal axis of hippocampus boosts prelimbic oscillations in the neonatal mouse

Joachim Ahlbeck, Lingzhen Song, Mattia Chini, Antonio Candela, Sebastian H. Bitzenhofer & Ileana L. Hanganu-Opatz

[1]*Developmental Neurophysiology, Institute of Neuroanatomy, University Medical Center Hamburg-Eppendorf, 20251 Hamburg, Germany*

Corresponding author: Ileana L. Hanganu-Opatz
Dev. Neurophysiology
Institute of Neuroanatomy
University Medical Center Hamburg-Eppendorf
Falkrenried 94
20251 Hamburg
Germany
phone: +49 40 7410 58966
fax: +49 40 7410 58925
e-mail: hangop@zmnh.uni-hamburg.de

Figures: 5
Number of pages: 35
Supplemental Material: 4 figures

Number of words in Summary: 149
Number of words in Introduction: 594
Number of words in Discussion: 1767

SUMMARY

The long-range coupling within prefrontal-hippocampal networks that account for cognitive performance emerges early in life. The discontinuous hippocampal theta bursts have been proposed to drive the generation of neonatal prefrontal oscillations, yet the cellular substrate of these early interactions is still unresolved. Here, we selectively target optogenetic manipulation of glutamatergic projection neurons in the CA1 area of either dorsal or intermediate/ventral hippocampus at neonatal age to elucidate their contribution to the emergence of prefrontal oscillatory entrainment. We show that despite stronger theta and ripples power in dorsal hippocampus, the prefrontal cortex is mainly coupled with intermediate/ventral hippocampus by phase-locking of neuronal firing via dense direct axonal projections. Theta band-confined activation by light of pyramidal neurons in intermediate/ventral but not dorsal CA1 that were transfected by *in utero* electroporation with high-efficiency channelrhodopsin boosts prefrontal oscillations. Our data causally elucidates the cellular origin of the long-range coupling in the developing brain.

Running title:

Optogenetic interrogation of early long-range coupling

Highlights:

- Neonatal theta bursts, sharp waves and ripples vary along septo-temporal axis
- Hippocampal activity times prefrontal oscillations via direct axonal projections
- Selective hippocampal targeting along septo-temporal axis causes precise firing
- Light stimulation of hippocampal neurons at 8 Hz boosts prefrontal oscillations

INTRODUCTION

In the adult rodent brain, coordinated patterns of oscillatory activity code in a frequency specific manner for sensory and cognitive performance. For example, learning and memory critically depend on oscillations within theta frequency band (4-12 Hz) that functionally couple the medial prefrontal cortex (PFC) and hippocampus (HP) (Siapas and Wilson, 1998; Benchenane et al., 2010; Brincat and Miller, 2015; Backus et al., 2016; Eichenbaum, 2017; Wirt and Hyman, 2017). These frequency-tuned brain states are present already during early development, long before the emergence of cognitive abilities, and have been extensively characterized and categorized according to their spatial and temporal structure (Lindemann et al., 2016). Network oscillations during development have a highly discontinuous and fragmented structure with bursts of activity alternating with “silent” periods (Hanganu et al., 2006; Seelke and Blumberg, 2010; Shen and Colonnese, 2016; Luhmann and Khazipov, 2017). The most common oscillatory pattern, spindle bursts, synchronizes large cortical and subcortical networks within theta-alpha frequency range. It is accompanied by slow delta waves as well as by faster discharges (beta and gamma oscillations) that account for local activation of circuits.

In the absence of direct behavioral correlates, a mechanistic understanding of oscillatory rhythms in the developing brain is currently lacking. In sensory systems, spindle bursts have been proposed to act as a template facilitating the formation of cortical maps (Dupont et al., 2006; Hanganu et al., 2006; Tolner et al., 2012), whereas early gamma oscillations seem to control the organization of thalamocortical topography (Minlebaev et al., 2011; Khazipov et al., 2013). In limbic systems dedicated to mnemonic and executive abilities, the knowledge on the relevance of early network oscillations is even sparser. Few lesion studies, yet without selectivity for specific activity patterns, suggested that prefrontal-hippocampal communication during development might be necessary for the maturation of episodic memory (Kruger et al., 2012). Temporal associations between the firing and synaptic discharges of individual neurons and network oscillations in different frequency bands gave first insights into the cellular substrate of coordinated activity in neonates.

Whereas in sensory systems, endogenous activation of sensory periphery drives entrainment of local circuitry through gap junction coupling as well as glutamatergic and GABAergic transmission (Dupont et al., 2006; Hanganu et al., 2006; Minlebaev et al., 2009), in developing prefrontal-hippocampal networks, the excitatory drive from the HP has been proposed to activate a complex layer- and frequency-specific interplay in the PFC (Brockmann et al., 2011; Bitzenhofer and Hanganu-Opatz, 2014; Bitzenhofer et al., 2015).

While most of this correlative evidence put forward the relevance of early oscillations beyond a simple epiphenomenal signature of developing networks, direct evidence for their causal contribution to circuit maturation is still missing. This is mainly due to the absence of a causal interrogation of developing networks, similarly to the investigations done in adult ones. Only recently the methodological difficulties related to area-, layer- and cell type-specific manipulations at neonatal age have been overcome (Bitzenhofer et al., 2017a; Bitzenhofer et al., 2017b). By these means, the local neuronal interplay generating beta-gamma oscillations in the PFC has been elucidated. However, the long-range coupling causing the activation of local prefrontal circuits is still unresolved. We previously proposed that the hippocampal CA1 area drives the oscillatory entrainment of PFC at neonatal age (Brockmann et al., 2011). Here, we developed a methodological approach to optically manipulate the neonatal HP along its septo-temporal axis. We provide causal evidence that theta frequency-specific activation of pyramidal neurons in the CA1 area of intermediate and ventral (i/vHP), but not of dorsal HP (dHP) elicits broad band oscillations in the PFC of neonatal mice via dense axonal projections.

RESULTS

Neonatal dorsal and intermediate / ventral hippocampus are differently entrained in discontinuous patterns of oscillatory activity

While different organization and function of dHP vs. i/vHP of adults have been extensively characterized (Thompson et al., 2008; Dong et al., 2009; Patel et al., 2013), their patterns of structural and functional maturation are still poorly understood. To fill this knowledge gap, we

firstly examined the network oscillatory and firing activity of CA1 area of either dHP or i/vHP by performing extracellular recordings of the local field potential (LFP) and multiple unit activity (MUA) in neonatal [postnatal day (P) 8-10] non-anesthetized and urethane-anesthetized mice (n=153). While urethane anesthesia led to an overall decrease of amplitude and power of oscillatory activity when compared to the non-anesthetized state of the same group of pups, the firing rate and timing as well as the synchrony and interactions within prefrontal-hippocampal networks were similar during both states (Figure S1). Due to the close proximity and the absence of reliable anatomical and functional borders between iHP and vHP at neonatal age, data from the two areas were pooled and referred as from i/vHP. The entire investigation was performed at the age of initiation of coupling between HP and PFC, i.e. P8-10 (Brockmann et al., 2011). Independent of the position along the dorsal-ventral axis, the CA1 area was characterized by discontinuous oscillations with main frequency in theta band (4-12 Hz) and irregular low amplitude beta-gamma band components, which have been previously categorized as theta oscillations (Brockmann et al., 2011). They were accompanied by prominent sharp-waves (SPWs) reversing across the pyramidal layer (str. pyr.) and by strong MUA discharge (Figures 1A, 1E). While the general patterns of activity were similar in dHP and i/vHP, their properties significantly differed between the sub-divisions. The theta bursts in i/vHP had significantly higher occurrence (i/vHP: 8.1 ± 0.2 oscillations/min, n=103 mice vs. dHP: 5.2 ± 0.3 oscillations/min, n=41 mice; $p<0.001$), larger amplitude (i/vHP:110.6 ± 5.6 µV vs. dHP: 92.9 ± 2.6 µV; $p=0.015$), and shorter duration (i/vHP: 3.5 ± 0.1 s vs. dHP: 4.3 ± 0.1 s, $p<0.001$) when compared with dHP (Figures 1B, S2A). Investigation of the spectral composition of theta bursts revealed significant differences within theta band with a stronger activation of dHP (relative power: dHP: 13.0 ± 1.3, n=41 mice; i/vHP: 10.3 ± 0.5, n=103 mice; $p=0.026$), whereas the faster frequency components were similar along the septo-temporal axis (relative power: 12-30 Hz: dHP, 15.0 ± 1.6, n=41 mice; i/vHP, 13.2 ± 0.7 n=103 mice, $p=0.22$; 30-100 Hz: dHP, 6.3 ± 0.6, n=41 mice; i/vHP: 5.2 ± 0.3, n=103 mice; $p=0.073$) (Figures 1C, S2B).

Differences along the septo-temporal axis were detected both in hippocampal spiking and population events SPWs. Overall, pyramidal neurons in i/vHP fired at higher rates (0.45 ± 0.01 Hz, n=557 units from 103 mice) than in the dHP (0.35 ± 0.02 Hz, n=158 units from 41 mice; p=0.025) (Figure 1D). Similar to adult HP (Patel et al., 2013), SPW in neonatal HP were more prominent in the dHP (712.8 ± 31.5 µV, n=41 mice) when compared with those occurring in the i/vHP (223.8 ± 6.3 µV, n=103 mice, p<0.001), yet their occurrence increased along the septo-temporal axis (dHP: 6.6 ± 0.5, n=41 mice; i/vHP: 8.6 ± 0.2, n=103 mice, p<0.001) (Figures 1E, 1F). In line with our previous results (Brockmann et al., 2011), SPWs were accompanied by prominent firing centered around the SPW peak (dHP, 232 units; i/vHP, 670 units) that were phase-locked to hippocampal ripples (Figure S2C). The power of ripples decreased along the septo-temporal axis (relative power: dHP, 24.4 ± 3.3, n=41 mice; i/vHP, 6.1 ± 0.60, n=103 mice, p<0.001) (Figures 1G, H). Similarly, the ripple-related spiking was stronger in dHP when compared with i/vHP (peak firing: dHP: 1.13 ± 0.09 Hz, n=232 units; i/vHP 0.84 ± 0.03, n=670, p<0.001) (Figures 1I, 1J).

These data show that the activity patterns in the dorsal and intermediate / ventral CA1 area differ in their properties and spectral structure.

Theta activity within dorsal and intermediate / ventral hippocampus differently entrains the neonatal prelimbic cortex

The different properties of network and neuronal activity in dHP vs. i/vHP led us to question their outcome for the long-range coupling in the developing brain. Past studies identified tight interactions between HP and PFC, which emerge already at neonatal age (Brockmann et al., 2011; Hartung et al., 2016) and are in support of memory at adulthood (Kruger et al., 2012; Spellman et al., 2015; Place et al., 2016). The discontinuous theta oscillations in HP have been proposed to drive the activation of local circuits in the PFC. To assess the coupling of dHP and i/vHP with PFC, we recorded simultaneously LFP and MUA in the corresponding hippocampal CA1 area and the prelimbic subdivision (PL) of the PFC of P8-10 mice. The entire investigation focused on PL, since in adults it is the prefrontal subdivision with the most dense innervation from HP (Jay and Witter, 1991; Vertes et al., 2007). In a first step, we

examined the temporal correspondence of discontinuous oscillations recorded simultaneously in the PL and dHP, as well as in the PL and i/vHP. We previously characterized the network activity in the PL and showed that spindle-shaped oscillations switching between theta (4-12 Hz) and beta-gamma (12-40 Hz) frequency components alternate with periods of silence (Brockmann et al., 2011; Cichon et al., 2014; Bitzenhofer et al., 2015). The majority of prelimbic and hippocampal oscillations co-occurred within a narrow time window (Figure 2A). The temporal synchrony between prelimbic and hippocampal oscillations was assessed by performing spectral coherence analysis (Figure 2B). The results revealed a stronger coupling for PL-i/vHP (4-12 Hz: 0.17 ± 0.0069; 12-30 Hz: 0.31 ± 0.011; 30-100 Hz: 0.11 ± 0.0069, n=103 mice) when compared with PL-dHP (4-12 Hz: 0.12 ± 0.0081; 12-30 Hz: 0.18 ± 0.0094; 30-100 Hz: 0.084 ± 0.004, n=41 mice). In line with previous investigations, this level of coherence is a genuine feature of investigated neonatal networks and not the result of non-specific and conduction synchrony, since we considered only the imaginary component of the coherence spectrum, which excludes zero time-lag synchronization (Nolte et al., 2004).

Due to the symmetric interdependence of coherence, it does not offer reliable insights into the information flow between two brain areas. Therefore, in a second step, we estimated the strength of directed interactions between PL and HP by calculating the generalized partial directed coherence (gPDC) (Baccala et al., 2007; Rodrigues and Baccala, 2016) (Figure 2C). The method bases on the notion of Granger causality (Granger, 1980) and avoids distorted connectivity results due to different scaling of data in HP and PL (Baccala et al., 2007; Taxidis et al., 2010). Independent of the position along the septo-temporal axis, the information flow in theta or beta frequency band from either dorsal or intermediate/ventral HP to PL was significantly stronger than in the opposite direction. However, mean gPDC values for i/vHP → PL were significantly ($p<0.001$) higher (0.069 ± 0.003, n=103 mice) when compared with those for dHP → PL (0.053 ± 0.003, n=41 mice). The stronger information flow from i/vHP to PL was confined to theta frequency range and was not detected for 12-30 Hz frequencies (i/vHP → PL: 0.048 ± 0.001; dHP → PL: 0.043 ± 0.002, p=0.16).

Correspondingly, the firing of individual prelimbic neurons was precisely timed by the phase of oscillations in i/vHP but not dHP (Figure 2D). Almost 20% of clustered units (52 out of 310 units) were locked to theta phase in i/vHP, whereas only 6.5% of units (3 out of 46 units) were timed by dHP. The low number of locked cells in dHP precluded the comparison of coupling strength between the two hippocampal sub-divisions.

These results indicate that the distinct activity patterns in dHP and i/vHP at neonatal age have different outcomes in their coupling with the PL. Despite higher power, theta oscillations in dHP do not substantially account for prelimbic activity. In contrast, i/vHP seems to drive neuronal firing and network entrainment in the PL.

SPWs-mediated output of intermediate / ventral but not dorsal hippocampus times network oscillations and spiking response in the neonatal prelimbic cortex

Since SPWs and ripples in dHP significantly differ from those in i/vHP, they might have a distinct impact on the developing PFC. While abundant literature documented the contribution of SPWs-spindles complex to memory-relevant processing in downstream targets, such as PFC (Colgin, 2011; Buzsaki, 2015; Colgin, 2016), it is unknown how these complexes affect the development of cortical activation. Simultaneous recordings from neonatal CA1 area either in dHP or i/vHP and PL showed that already at neonatal age, prefrontal oscillations are generated shortly (~100 ms) after hippocampal SPWs - ripples. This prelimbic activation is significantly stronger when induced by SPWs-ripples emerging in i/vHP than in dHP as reflected by the significantly higher power of oscillatory activity in theta (PL for dHP: 186.9 ± 12.5 μV^2; PL for i/vHP: 249.5 ± 14.5 μV^2, p=0.0088), beta (PL for dHP: 34.3 ± 3.3 μV^2; PL for i/vHP: 48.1 ± 2.8 μV^2, p=0.0049), and gamma (PL for dHP: 11.3 ± 0.9 μV^2; PL for i/vHP: 17.4 ± 1.2 μV^2, p=0.0026) frequency band (Figure 3A). The SPWs-ripple-induced oscillatory activity in the PL of neonatal mice was accompanied by augmentation of firing rates. While the induced firing in i/vHP peaked (≈90 ms) after SPWs-ripples and remained significantly ($p<0.001$) elevated for several seconds, a less prominent peak was observed following SPW-ripples in dHP (Figures 3B, 3C).

These data reveal that SPWs-ripples from intermediate / ventral but less from the dorsal part of hippocampal CA1 correlate with pronounced neuronal firing and local entrainment in the PL of neonatal mice.

Pyramidal neurons in intermediate / ventral but not dorsal hippocampus densely project to the prefrontal cortex at neonatal age

To identify the anatomical substrate of different coupling strength between i/vHP - PL and dHP - PL, we monitored the projections that originate from the CA1 area in both hippocampal subdivisions and target the PFC. The direct unilateral projections from hippocampal CA1 area to PL have been extensively investigated in adult brain (Swanson, 1981; Jay and Witter, 1991; Vertes et al., 2007) and are present already at neonatal age (Brockmann et al., 2011; Hartung et al., 2016). We tested for sub-division specific differences by using retrograde and anterograde tracing. First, we injected unilaterally small amounts of the retrograde tracer Fluorogold (FG) into the PL of P7 mice (n=8 mice). Three days after FG injections, labeled cells were found in str. pyr. of CA1 in both dHP and i/vHP (Figure 4A). However, their density was significantly different ($p<0.001$); whereas in dHP very few cells were retrogradely labeled ($0.15*10^3 \pm 0.074*10^3$ cells/mm^2), a large proportion of pyramidal-shaped cells in the CA1 area of i/vHP projects to PL ($3.29*10^3 \pm 0.19*10^3$ cells/mm^2).

Second, the preferential innervation of PL by pyramidal neurons from CA1 area of i/vHP was confirmed by anterograde staining with BDA (n=9 mice). Small amounts of BDA were injected into the CA1 area of i/vHP (Figure 4B). They led to labeling of the soma and arborized dendritic tree of pyramidal neurons in str. pyr. with the characteristic orientation of axons. In 7 out of 9 mice anterogradely-labeled axons were found in the PL, preferentially within its deep layers V and VI.

Thus, the dense axonal projections from CA1 area of i/vHP might represent the substrate of HP-induced oscillatory entrainment of prelimbic circuits.

Selective light activation of pyramidal neurons in CA1 area of intermediate / ventral but not dorsal hippocampus causes frequency-specific entrainment of neonatal prelimbic circuits

The tight coupling by synchrony and the directed information flow from hippocampal CA1 area to PL via direct axonal projections suggest that the HP acts already at neonatal age as a drive for prelimbic activation. Moreover, the differences identified between the dHP – PL and i/vHP – PL communication argue for prominent augmentation of driving force along the septo-temporal hippocampal axis. To causally confirm these correlative evidences, we selectively activated by light the pyramidal neurons in the CA1 area of either dHP or i/vHP that had been transfected with a highly efficient fast-kinetics double mutant ChR2E123T/T159C (ET/TC) (Berndt et al., 2011) and the red fluorescent protein tDimer2 by *in utero* electroporation (IUE) (Figure S3A). This method enables stable area and cell type-specific transfection of neurons already prenatally without the need of cell-type specific promotors of a sufficiently small size (Baumgart and Grebe, 2015; Szczurkowska et al., 2016). To target neurons along the septo-temporal axis, distinct transfection protocols were used. When the IUE was performed with two paddles placed 25° leftward angle from the midline and a 0° angle downward from anterior to posterior, tDimer-positive neurons were mainly found in the CA1 area of the dHP, as revealed by the analysis of consecutive coronal sections from IUE-transfected P8-10 mice. Targeting of i/vHP succeeded only when three paddles were used, with both positive poles located at 90° leftward angle from the midline and the third negative pole at 0° angle downward from anterior to posterior (Figures 5A, S2B). Staining with NeuN showed that a substantial proportion of neurons in str. pyr. of CA1 area (dHP: 18.3 ± 1.0%; n=36 slices from 13 mice; i/vHP: 14.5 ± 1.5%, n=12 slices from 11 mice) were transfected by IUE. The shape of tDimer2-positive neurons, the orientation of primary dendrites, and the absence of positive staining for GABA confirmed that the light-sensitive protein ChR2(ET/TC) was integrated exclusively into cell lineages of pyramidal neurons (Figure 5A). Omission of ChR2(ET/TC) from the expression construct (i.e. opsin-free) yielded similar expression rates and distribution of tDimer2-positive neurons (Figure S3C).

To exclude non-specific effects of transfection procedure by IUE on the overall development of mice, we assessed the developmental milestones and reflexes of electroporated opsin-expressing and opsin-free mice (Figure S3D). While IUE caused significant reduction of litter size (non-electroporated 6.5 ± 0.7 pups/litter, electroporated: 4.5 ± 0.5 pups/litter, p=0.017), all investigated pups had similar body length, tail length, and weight during early postnatal period. Vibrissa placing, surface righting and cliff aversion reflexes were also not affected by IUE or transfection of neurons with opsins. These data indicate that the overall somatic development during embryonic and postnatal stage of ChR2(ET/TC)-transfected mice is unaltered.

We first assessed the efficiency of light stimulation in evoking action potentials in neonatal hippocampal neurons *in vivo*. Blue light pulses (473 nm, 20-40 mW/mm^2) at different frequencies (4, 8, 16 Hz) led shortly (<10 ms) after the stimulus to precisely timed firing of transfected neurons in both dHP and i/vHP. Our previous experimental data and modeling work showed that the used light power did not cause local tissue heating that might interfere with neuronal spiking (Stujenske et al., 2015; Bitzenhofer et al., 2017b). For both hippocampal sub-divisions the efficiency of firing similarly decreased with augmenting frequency (Figure 5B). For stimulation frequencies >16 Hz, the firing lost the precise timing by light, most likely due to the immaturity of neurons and their projections.

To decide whether activation of HP drives frequency-specific oscillatory activity and boosts the entrainment of prelimbic circuits, we simultaneously performed multi-site recordings of LFP and MUA in PL and HP during pulsed light stimulation of CA1 area of dHP (n=22 mice) or i/vHP (n=9 mice) (Figure 5C). The firing in i/vHP timed by light at 8 Hz, but not at 4 Hz or 16 Hz, caused significant (theta: p=0.039, beta: p=0.030, gamma: p=0.0036) augmentation of oscillatory activity in all frequency bands as reflected by the higher power in the PL during the stimulation when compared with the time window before the train of pulses (Figure 5D, table 1). In contrast, stimulation by light of dHP left the prelimbic activity unaffected. In opsin-free animals, stimulation of dHP and i/vHP led to no significant changes in the oscillatory activity (Figure S4A, table 1). Rhythmic firing of prelimbic neurons was not

306 detected after light activation of hippocampal subdivisions, most likely because hippocampal
307 axons mainly target the deep layers of PL /s. above) and the recordings were performed from
308 layer II/III.

309 Thus, theta band entrainment of pyramidal neurons in the CA1 area of i/vHP but not
310 dHP caused broad activation of local circuits in PL.

311

312 **DISCUSSION**

313 Combining selective optogenetic activation with extracellular recordings and tracing of
314 projections in neonatal mice *in vivo*, we provide causal evidence that theta activity in the CA1
315 area of i/vHP but not dHP drives network oscillations within developing prefrontal cortex.
316 Despite stronger theta power in the dHP, solely optical activation of the pyramidal neurons in
317 i/vHP at theta frequency range (8 Hz) boosted the emergence of discontinuous oscillatory
318 activity in theta and beta-gamma bands in the neonatal PFC. These data identifies the
319 cellular substrate of the directed interactions between neonatal hippocampus and prefrontal
320 cortex and offer new perspectives for the interrogation of long-range coupling in the
321 developing brain and its behavioral readout.

322

323 ***Distinct patterns of functional maturation in dorsal and intermediate / ventral***
324 ***hippocampus***

325 The abundant literature dedicated to the adult hippocampus mainly deals with a single
326 cortical module (Amaral et al., 2007). However, an increasing number of studies in recent
327 years revealed distinct organization, processing mechanisms and behavioral relevance for
328 dHP vs. i/vHP (Fanselow and Dong, 2010; Bannerman et al., 2014; Strange et al., 2014). For
329 example, the dHP, which receives dense projections from the entorhinal cortex (Witter and
330 Amaral, 2004), is mainly involved in spatial navigation (O'Keefe and Nadel, 1978; Moser et
331 al., 1995; Moser, 1998). In contrast, the ventral part receives strong cholinergic and
332 dopaminergic innervation (Witter et al., 1989; Pitkanen et al., 2000) and contributes to
333 processing of non-spatial information (Bannerman et al., 2003; Bast et al., 2009).
334 Correspondingly, the network and neuronal activity changes along the septo-temporal axis.

335 The power of the most prominent activity pattern in the adult HP, the theta oscillations, as
336 well as the theta timing of the neuronal firing was found to be substantially reduced in the
337 i/vHP when compared with dHP (Royer et al., 2010). By these means, the precise spatial
338 representation deteriorates along the septo-temporal axis, since theta activity is directly
339 linked to place cell representation (O'Keefe and Recce, 1993; Geisler et al., 2007). In
340 contrast, SPWs are more prominent and ripples have higher amplitude and frequency in the
341 ventral HP than in the dHP (Patel et al., 2013).

342 Our data uncovered that some of these differences in the activity patterns along the
343 septo-temporal axis emerge already during early neonatal development. Similar to findings
344 from adult rodents, the power of theta bursts at neonatal age was higher in dHP than in
345 i/vHP. The amplitude of SPWs and the power of ripples decreased along the septo-temporal
346 axis. These findings give insights into the mechanisms underlying the early generation of
347 activity patterns. It has been proposed that the differences in theta dynamics along the septo-
348 temporal axis result from distinct innervation, on the one hand, and from specific intrinsic
349 properties of hippocampal neurons, on the other hand. Cholinergic projections of different
350 origin in the dHP and i/vHP (Stewart and Fox, 1990; Amaral et al., 2007) as well as
351 maturational differences in the intrinsic resonant properties of hippocampal neurons and
352 notable gradients of parvalbumin immunoreactivity along the septo-temporal axis (Honeycutt
353 et al., 2016) may contribute to the observed differences.

354 Quantification along the septo-temporal axis relevealed that, similar to adults, the
355 occurrence of SPWs was higher in the i/vHP and their amplitude was larger in the neonatal
356 dHP (Patel et al., 2013). It is still an issue of debate when exactly ripples emerge in the
357 developing hippocampus, although it is obvious that they appear later than theta bursts and
358 SPWs, most likely towards the end of the first and during second postnatal week (Buhl and
359 Buzsaki, 2005; Brockmann et al., 2011). Their underlying mechanisms at neonatal age
360 remain also largely unknown and need to be related to age-dependent changes in gap
361 junctional coupling and GABA switch (Ben-Ari et al., 1989; Zhang et al., 1990; Yuste et al.,
362 1995). The organization of SPWs and ripples is of particular relevance when considering

their impact on the early activity of PFC. Already at neonatal age, the prelimbic firing and oscillatory entrainment is timed by SPWs-ripples. Of note, the degree of timing varies along the septo-temporal axis and is much higher for the i/vHP.

Optogenetic interrogation of long-range coupling in the developing brain

At adult age the communication between PFC and HP has been investigated in relationship with memory tasks both under physiological and disease-related conditions (Sirota et al., 2008; Adhikari et al., 2010; Sigurdsson et al., 2010; Eichenbaum, 2017). Depending on the phase of memory processing, the prefrontal-hippocampal coupling via oscillatory synchrony has been found to be either unidirectional from the HP to PFC or bidirectional (Siapas et al., 2005; Hallock et al., 2016; Place et al., 2016). Both theta and gamma network oscillations contribute to the functional long-range coupling. The model of prefrontal-hippocampal communication has been initially built based on experimental evidence correlating the temporal organization of neuronal and network activity in the two brain areas. The time delay between spike trains and oscillatory phase or between oscillations enabled to propose that the information flows in one direction or the other via mono- or polysynaptic axonal projections. More recently, a direct causal assessment of the coupling became possible through optogenetic interrogation of neural circuits. In a seminal study, Spellman and colleagues used light-driven inhibition of axonal terminals for dissecting the directionality of interactions between PFC and HP during different phases of memory retrieval (Spellman et al., 2015).

We previously showed that at neonatal age, long before the maturation of cognitive abilities, discontinuous theta bursts in i/vHP are temporally correlated to the network oscillations in the PFC and time the prefrontal firing (Brockmann et al., 2011; Hartung et al., 2016). Moreover, the temporal delay of 10-20 ms between prefrontal and hippocampal spike trains as well as the estimated directionality of information flow between the two areas suggested that hippocampal theta drives the oscillatory entrainment of the local circuits in the PFC. The present data directly prove this hypothesis, taking advantage of the recently

developed protocol for optogenetic manipulation of neuronal networks at neonatal age (Bitzenhofer et al., 2017a; Bitzenhofer et al., 2017b).

Several considerations regarding the technical challenges of optogenetic manipulation of HP along the septo-temporal axis need to be made. Besides the inherent difficulties related to the specificity of promoters for selective transfection and the targeting procedure that are ubiquitary for all developing networks and have been addressed elsewhere (Bitzenhofer et al., 2017a), confinement of light-sensitive proteins to pyramidal neurons of either dHP or i/vHP required special attention. In a previous study (Bitzenhofer et al., 2017b), we developed a selective targeting protocol of neonatal neurons that relies on the combination of CAG promoter and IUE. By these means, the expression of light-sensitive proteins in the neurons located in the neocortical layer and area of interest was sufficiently high to ensure their reliable activation. Similarly, the expression of ChR2(ET/TC) in the pyramidal neurons of hippocampal CA1 area under the CAG promoter was sufficiently high to reliably cause network and neuronal activity. Taking into account that viral transduction, which usually requires 10-14 days for stable expression, is only of limited usability to investigate local network interactions during development, IUE seems to represent the method of choice for manipulating circuits at this early age. IUE enables targeting of precursor cells of neuronal and glial subpopulations, based on their distinct spatial and temporal patterns of generation in the ventricular zone (Tabata and Nakajima, 2001; Borrell et al., 2005; Niwa et al., 2010; Hoerder-Suabedissen and Molnar, 2015). IUE based on 2 electrode paddles enabled selective targeting of pyramidal neurons in the CA1 area of dHP in more than half of the pups per litter (Figure S3(i)), but it completely failed (0 out of 32 mice) to target these neurons in i/vHP. Therefore, it was necessary to use a modified IUE protocol based on three electrodes. This protocol, although more complicated and time consuming, allows reliable transfection at brain locations that are only able to be sporadically targeted by two electrodes The high IUE-induced expression of light sensitive proteins enables the reliable firing of neurons in both dHP and i/vHP in response to light pulses. One intriguing question is how many pyramidal neurons in str. pyr. of CA1 area must be

synchronously activated to drive the oscillatory entrainment of prelimbic circuitry. Anterograde and retrograde tracing demonstrated the density increase along the septo-temporal axis of hippocampal axons targeting the PL. Light activation / inhibition of these axonal terminals paired with monitoring of network oscillations in the PFC might offer valuable insights into the patterns of coupling sufficient for activation.

Functional relevance of frequency-specific drive within developing prefrontal-hippocampal networks

Abundant literature links theta frequency coupling within prefrontal-hippocampal networks to cognitive performance and emotional states of adults (Adhikari et al., 2010; Xu and Sudhof, 2013; Spellman et al., 2015; Hallock et al., 2016; Place et al., 2016; Ye et al., 2017). The early emergence of directed communication between PFC and i/vHP raises the question of functional relevance of this early coupling during development and at adulthood.

The maturation of cognitive abilities is a process even more protracted than sensory development and starts during second-third postnatal week (Hanganu-Opatz, 2010; Cirelli and Tononi, 2015). Some of these abilities, such as recognition memory, can be easily monitored at early age and seems to critically rely on structurally and functionally intact prefrontal-hippocampal networks (Kruger et al., 2012). Direct assessment of the role of neonatal communication for memory performance as performed for adult circuits is impossible due to the temporal delay of the two processes. The alternative is to manipulate the activity of either PFC, HP or the connectivity between them during defined developmental time windows and monitor the juvenile and adult consequences at structural, functional and behavioral levels. The present data and optogenetic protocol represent the pre-requisite of this investigation, opening new perspectives for assessing the adult behavioral readout of long-range communication in the developing brain.

One question that remains to be addressed is how the hippocampal theta drive shapes the maturation of prefrontal-hippocampal networks. Following the general rules of activity-dependent plasticity (Hubel et al., 1977; Huberman et al., 2006); (Xu et al., 2011;

Yasuda et al., 2011), the precisely timed excitatory inputs from the i/vHP to the PL might facilitate the wiring of local prefrontal circuitry and enable the refinement of behaviorally relevant communication scaffold between the two regions. By these means, the prefrontal activity driven by projection neurons in the HP act as a template, having a pre-adaptive function that facilitates the tuning of circuits with regard to future conditions. This instructive role of theta activity for the prefrontal circuits needs to be proven by manipulation of temporal structure of the hippocampal drive without affecting the overall level of activity. Understanding the rules that govern the early organization of large-scale networks represents the pre-requisite for identifying the structural and functional deficits related to abnormal behavior and disease.

MATERIALS AND METHODS

Experimental model and subject details

Mice. All experiments were performed in compliance with the German laws and the guidelines of the European Community for the use of animals in research and were approved by the local ethical committee (111/12, 132/12). Timed-pregnant C57Bl/6J mice from the animal facility of the University Medical Center Hamburg-Eppendorf were housed individually in breeding cages at a 12 h light / 12 h dark cycle and fed *ad libitum*. The day of vaginal plug detection was defined E0.5, while the day of birth was assigned as P0. Both female and male mice underwent light stimulation and multi-site electrophysiological recordings at P8-10 after transfection with light-sensitive proteins by IUE at E15.5. For monitoring of projections, tracers were injected at P7 and monitored in their distribution along the axonal tracts at P10.

Methods details

Surgical procedures

In utero electroporation. Starting one day before and until two days after surgery, timed-pregnant C57Bl/6J mice received on a daily basis additional wet food supplemented with 2-4 drops Metacam (0.5 mg/ml, Boehringer-Ingelheim, Germany). At E15.5 randomly assigned pregnant mice were injected subcutaneously with buprenorphine (0.05 mg/kg body weight)

30 min before surgery. The surgery was performed on a heating blanket and toe pinch and breathing were monitored throughout. Under isoflurane anesthesia (induction: 5%, maintenance: 3.5%) the eyes of the dam were covered with eye ointment to prevent damage before the uterine horns were exposed and moistened with warm sterile phosphate buffered saline (PBS, 37°C). Solution containing 1.25 µg/µl DNA [pAAV-CAG-ChR2(E123T/T159C)-2A-tDimer2, or pAAV-CAG-tDimer2)] (Figure S3A) and 0.1% fast green dye at a volume of 0.75-1.25 µl were injected into the right lateral ventricle of individual embryos using pulled borosilicate glass capillaries with a sharp and long tip. Plasmid DNA was purified with NucleoBond (Macherey-Nagel, Germany). 2A encodes for a ribosomal skip sentence, splitting the fluorescent protein tDimer2 from the opsin during gene translation. Two different IUE protocols were used to target pyramidal neurons in CA1 area of either dHP or i/vHP. To target dHP, each embryo within the uterus was placed between the electroporation tweezer-type paddles (5 mm diameter, Protech, TX, USA) that were oriented at a 25° leftward angle from the midline and a 0° angle downward from anterior to posterior. Electrode pulses (35 V, 50 ms) were applied five times at intervals of 950 ms controlled by an electroporator (CU21EX, BEX, Japan) (Figure S3B(i)) (Baumgart and Grebe, 2015). To target i/vHP, a tri-polar approach was used (Szczurkowska et al., 2016). Each embryo within the uterus was placed between the electroporation tweezer-type paddles (5 mm diameter, both positive poles, Protech, TX, USA) that were oriented at 90° leftward angle from the midline and a 0° angle downward from anterior to posterior. A third custom build negative pole was positioned on top of the head roughly between the eyes. Electrode pulses (30 V, 50 ms) were applied six times at intervals of 950 ms controlled by an electroporator (CU21EX, BEX, Japan) (Figure S3B(ii)). By these means, neural precursor cells from the subventricular zone, which radially migrate into the HP, were transfected. Uterine horns were placed back into the abdominal cavity after electroporation. The abdominal cavity was filled with warm sterile PBS (37°C) and abdominal muscles and skin were sutured individually with absorbable and non-absorbable suture thread, respectively. After recovery, pregnant mice were returned to their home cages, which were half placed on a heating blanket for two days after surgery.

Retrograde and anterograde tracing. For retrograde tracing, mice were injected at P7 with Fluorogold (Fluorochrome, LLC, USA) unilaterally into the PFC using iontophoresis. The pups were placed in a stereotactic apparatus and kept under anesthesia with isoflurane (induction: 5%, maintenance: 2.5%) for the entire procedure. A 10 mm incision of the skin on the head was performed with small scissors. The bone above the PFC (0.5 mm anterior to bregma, 0.3 mm right to the midline) was carefully removed using a syringe. A glass capillary (≈20 µm tip diameter) was filled with ≈1 µL of 5% Fluorogold diluted in sterile water by capillary forces, and a silver wire was inserted such that it was in contact with the Fluorogold solution. For anterograde tracing, mice were injected at P7 with the anterograde tracer biotinylated dextran amine (BDA) (Thermo Fisher Scientific, USA) unilaterally into i/vHP using iontophoresis and surgery protocols as described above. The bone above i/vHP (0.7 mm anterior to lambda, 2-3 mm right to the midline) was carefully removed using a syringe. A glass capillary (≈30 µm tip diameter) was filled with ≈1 µL of 5% BDA diluted in 0.125 M phosphate buffer by capillary forces, and a silver wire was inserted such that it was in contact with the BDA solution. For both anterograde and retrograde tracing, the positive pole of the iontophoresis device was attached to the silver wire, the negative one was attached to the skin of the neck. The capillary was carefully lowered into the PFC (≈1.5 mm dorsal from the dura) or HP (≈1.5 mm dorsal from the dura). Iontophoretically injection by applying anodal current to the pipette (6s on/off current pulses of 6 µA) was done for 5 min. Following injection, the pipette was left in place for at least 5 min and then slowly retracted. The scalp was closed by application of tissue adhesive glue and the pups were left on a heating pad for 10-15 minutes to fully recover before they were given back to the mother. The pups were perfused at P10.

Surgical preparation for acute electrophysiological recording and light delivery. For recordings in non-anesthetized state, 0.5% bupivacain / 1% lidocaine was locally applied on the neck muscles. For recordings under anesthesia, mice were injected i.p. with urethane (1 mg/g body weight; Sigma-Aldrich, MO, USA) prior to surgery. For both groups, under isoflurane anesthesia (induction: 5%, maintenance: 2.5%) the head of the pup was fixed into

a stereotaxic apparatus using two plastic bars mounted on the nasal and occipital bones with dental cement. The bone above the PFC (0.5 mm anterior to bregma, 0.5 mm right to the midline for layer V/VI), hippocampus (2.0 mm posterior to bregma, 1.0 mm right to the midline for dHP, 3.5 mm posterior to bregma, 3.5 mm right to the midline for i/vHP) was carefully removed by drilling a hole of <0.5 mm in diameter. After a 10-20 min recovery period on a heating blanket mice were moved to the setup for electrophysiological recording. Throughout the surgery and recording session the mouse was positioned on a heating pad with the temperature kept at 37°C.

Perfusion. Mice were anesthetized with 10% ketamine (aniMedica, Germany) / 2% xylazine (WDT, Germany) in 0.9% NaCl solution (10 µg/g body weight, i.p.) and transcardially perfused with Histofix (Carl Roth, Germany) containing 4% paraformaldehyde for 30-40 minutes. Brains were postfixed in 4% paraformaldehyde for 24 h.

Behavioral testing

Examination of developmental milestones. Mouse pups were tested for their somatic development and reflexes at P2, P5 and P8. Weight, body and tail length were assessed. Surface righting reflex was quantified as time (max 30 s) until the pup turned over with all four feet on the ground after being placed on its back. Cliff aversion reflex was quantified as time (max 30 s) until the pup withdrew after snout and forepaws were positioned over an elevated edge. Vibrissa placing was rated positive if the pup turned its head after gently touching the whiskers with a toothpick.

Electrophysiology

Electrophysiological recording. A one-shank electrode (NeuroNexus, MI, USA) containing 1x16 recording sites (0.4-0.8MΩ impedance, 100 mm spacing) was inserted into the PFC. One-shank optoelectrodes (NeuroNexus, MI, USA) containing 1x16 recordings sites (0.4-0.8 MΩ impedance, 50 mm spacing) aligned with an optical fiber (105 mm diameter) ending 200 µm above the top recording site was inserted into either dHP or i/vHP. A silver wire was inserted into the cerebellum and served as ground and reference electrode. A recovery period of 10 min following insertion of electrodes before acquisition of data was provided.

559 Extracellular signals were band-pass filtered (0.1-9,000 Hz) and digitized (32 kHz) with a
560 multichannel extracellular amplifier (Digital Lynx SX; Neuralynx, Bozeman, MO, USA) and
561 the Cheetah acquisition software (Neuralynx). Spontaneous (i.e. not induced by light
562 stimulation) activity was recorded for 15 min at the beginning and end of each recording
563 session as baseline activity. Only the baseline prior to stimulation epochs was used for data
564 analysis.

565 *Light stimulation.* Pulsed (laser on-off) light stimulations were performed with an arduino uno
566 (Arduino, Italy) controlled diode laser (473 nm; Omicron, Austria). Laser power was adjusted
567 to trigger neuronal spiking in response to >25% of 3-ms-long light pulses at 16 Hz. Resulting
568 light power was in the range of 20-40mW/mm^2 at the fiber tip. For each frequency used (4, 8
569 and 16 Hz), stimuli (3 ms pulse length, 3 s stimulation duration, 6 s inter stimulation interval)
570 were repeated (30 times) in a randomized order.

571 ***Histology***

572 *Immunohistochemistry*. Brains were sectioned coronally at 50 µm. Free-floating slices were
573 permeabilized and blocked with PBS containing 0.2 % Triton X 100 (Sigma-Aldrich, MO,
574 USA), 10 % normal bovine serum (Jackson Immuno Research, PA, USA) and 0.02% sodium
575 azide. Subsequently, slices were incubated overnight with mouse monoclonal Alexa Fluor-
576 488 conjugated antibody against NeuN (1:200, MAB377X, Merck Millipore, MA, USA) or
577 rabbit polyclonal primary antibody against GABA (1:1,000, A2052; Sigma-Aldrich), followed
578 by 2 h incubation with Alexa Fluor-488 goat anti-rabbit IgG secondary antibody (1:500,
579 A11008; Merck Millipore). Slices were transferred to glass slides and covered with
580 Fluoromount (Sigma-Aldrich, MO, USA).

581 For 3.3'-diaminobenzidie (DAB) staining sections (prepared as described above) were rinsed
582 in PBS (0.125 M, pH 7.4–7.6) for 10 min, treated with peroxide solution (3% peroxide, 10%
583 methanol in 0.125 M PB) for 10 min to quench any endogenous peroxidases within the
584 tissue, and rinsed again. Subsequently, the sections were washed in PBS containing 0.5%
585 Triton-X and incubated with avidin biotinylated enzyme complex (ABC, VECTASTAIN ABC
586 Kit, USA) at room temperature or overnight at 4°C. After rinsing in Tris-HCl (pH 7.4), the

sections were further incubated with DAB working buffer (DAB peroxidase substrate kit, Vector Laboratories, USA) at room temperature for 2-10 min. After the signal was detected, all sections were rinsed with Tris-HCl.

Imaging. Wide field fluorescence was performed to reconstruct the recording electrode position in brain slices of electrophysiologically investigated pups and to localize tDimer2 expression in pups after IUE. High magnification images were acquired with a confocal microscope (DM IRBE, Leica, Germany) to quantify tDimer2 expression and immunopositive cells (1-4 brain slices / investigated mouse). For DAB staining, brightfield images were obtained using Zeiss imager M1 microscope (Zeiss, Oberkochen, Germany) and enhanced using the National Institutes of Health (NIH) Image program.

Quantification and statistical analysis

Immunohistochemistry quantification. All images were similarly analyzed with ImageJ. For quantification of fluorogold tracing automatic cell counting was done using custom-written tools. To quantify tDimer2, NeuN and GABA-positive neurons, manual counting was performed, since the high neuronal density in str. pyr. prevented reliable automatic counting.

Spectral analysis of LFP. Data were imported and analyzed offline using custom-written tools in the Matlab environment (MathWorks). Data were processed as following: band-pass filtered (500–5,000 Hz) to analyze MUA and low-pass filtered (<1,400 Hz) using a third-order Butterworth filter before downsampling to 3.2 kHz to analyze LFP. All filtering procedures were performed in a manner preserving phase information.

Detection of oscillatory activity. The detection and of discontinuous patterns of activity in the neonatal PL and HP were performed using a modified version of the previously developed algorithm for unsupervised analysis of neonatal oscillations (Cichon et al., 2014) and confirmed by visual inspection. Briefly, deflections of the root mean square of band-pass filtered signals (1–100 Hz) exceeding a variance-depending threshold were assigned as network oscillations. The threshold was determined by a Gaussian fit to the values ranging from 0 to the global maximum of the root-mean-square histogram. If two oscillations occurred

within 200 ms of each other they were considered as one. Only oscillations lasting > 1 s was included.

Detection of sharpwaves. Sharpwaves were detected by subtracting the filtered signal (1-300 Hz) from the recording sites 100 µm above and 100 µm below the recording site in str. pyr. Sharpwaves were then detected as peaks above 5 times the standard deviation of the subtracted signal.

Power spectral density. Power spectral density was calculated using the Welch's method. Briefly, segments of the recorded signal were glued together (1 s segments for oscillatory activity; 300 ms segments for sharpwave pre/post comparison; 100 ms segments for ripple comparison; 3 s for light evoked activity) and power were then calculated using non-overlapping windows. Time–frequency plots were calculated by transforming the data using Morlet continuous wavelet.

Coherence. Coherence was calculated using the imaginary coherency method (Nolte et al., 2004). Briefly, the imaginary coherence was calculated by taking the imaginary component of the cross-spectral density between the two signals and normalized by the power spectral density of each. The computation of the imaginary coherence C over frequency (f) for the power spectral density P of signal X and Y was performed according to the formula:

$$C_{XY}(f) = Im\left(\frac{|P_{XY}(f)|^2}{P_{XX}(f)P_{YY}(f)}\right)$$

General partial directed coherence. gPDC is based on linear Granger causality measure. The method attempts to describe the causal relationship between multivariate time series based on the decomposition of multivariate partial coherences computed from multivariate autoregressive models. The LFP signal was divided into segments containing the oscillatory activity. Signal was de-noised using wavelets with the Matlab wavelet toolbox. After de-noising, gPDC was calculated using the gPDC algorithm previously described (Baccala et al., 2007).

Single unit activity analysis. SUA was detected and clustered using Offline Sorter (Plexon, TC, USA). 1–4 single units were detected at each recording site. Subsequently, data were imported and analyzed using custom-written tools in the Matlab software (MathWorks). The firing rate temporally related to SPWs was calculated by aligning all units to the detected SPWs. For assessing the phase locking of units to LFP, we firstly used the Rayleigh test for non-uniformity of circular data to identify the units significantly locked to network oscillations. The phase was calculated by extracting the phase component using the Hilbert transform of the filtered signal at each detected spike. Spikes occurring in a 15 ms-long time window after the start of a light pulse were considered to be light-evoked. Stimulation efficacy was calculated as the probability of at least one spike occurring in this period.

Statistical analysis. Statistical analyses were performed using SPSS Statistics 21 (IBM, NY, USA) or Matlab. Data were tested for normal distribution by the Shapiro–Wilk test. Normally distributed data were tested for significant differences (*p<0.05, **p<0.01 and ***p<0.001) using paired t-test, unpaired t-test or one-way repeated-measures analysis of variance with Bonferroni-corrected post hoc analysis. Not normally distributed data were tested with the nonparametric Mann–Whitney U-test. The circular statistics toolbox was used to test for significant differences in the phase locking data. Data are presented as mean ± SEM. No statistical measures were used to estimate sample size since effect size was unknown. Investigators were not blinded to the group allocation during the experiments. Unsupervised analysis software was used if possible to preclude investigator biases. Summary of performed statistical analysis is summarized in table S1.

Major datasets

Author	Year	Dataset title	Dataset URL	Database, license and accessibility information
Ahlbeck et al.,	2017	Data from: Glutamatergic drive along the septo-temporal axis of hippocampus boosts prelimbic oscillations in the neonatal mouse	https://doi.org/10.5061/dryad.52fh7	Available at Dryad Digital Repository under a CC0 Public Domain Dedication

663

664 **Author contributions**

665 I.L.H.-O. designed the experiments, J.A., L.S., M.C., S.H.B. and A.C. carried out the
666 experiments, J.A. and M.C., analyzed the data, I.L.H.-O. and J.A. interpreted the data and
667 wrote the paper. All authors discussed and commented on the manuscript.

668

669 **Acknowledgments**

670 We thank Nadine Faesel for the establishment of tracing technique, Drs. L. Cancedda and A.
671 Cwetsch for help with the *in utero* electroporation, Drs. S. Wiegert, T. Oertner, and C. Gee
672 for help with the development of opsin constructs as well as A. Marquardt, P. Putthoff, A.
673 Dahlmann and I. Ohmert for excellent technical assistance.

674 I.L.H.-O. acknowledges support by the ERC (ERC Consolidator Grant 681577) and by the
675 German Research Foundation (SFB 936 (B5) and SPP 1665 (Ha4466/12-1)).

676 I.L.H.-O. is member of the FENS Kavli Network of Excellence.

677 *In memoriam of Howard Eichenbaum*

678

679 **Competing interests**

680 The authors declare no competing financial interests.

681

REFERENCES

Adhikari, A., Topiwala, M.A., and Gordon, J.A. (2010). Synchronized activity between the ventral hippocampus and the medial prefrontal cortex during anxiety. *Neuron* 65(2), 257-269. doi: 10.1016/j.neuron.2009.12.002.

Amaral, D.G., Scharfman, H.E., and Lavenex, P. (2007). The dentate gyrus: fundamental neuroanatomical organization (dentate gyrus for dummies). *Prog Brain Res* 163, 3-22. doi: 10.1016/S0079-6123(07)63001-5.

Baccala, L.A., Sameshima, K., and Takahashi, D.Y. (Year). "Generalized Partial Directed Coherence", in: *2007 15th International Conference on Digital Signal Processing*), 163-166.

Backus, A.R., Schoffelen, J.M., Szebenyi, S., Hanslmayr, S., and Doeller, C.F. (2016). Hippocampal-Prefrontal Theta Oscillations Support Memory Integration. *Curr Biol* 26(4), 450-457. doi: 10.1016/j.cub.2015.12.048.

Bannerman, D.M., Grubb, M., Deacon, R.M.J., Yee, B.K., Feldon, J., and Rawlins, J.N.P. (2003). Ventral hippocampal lesions affect anxiety but not spatial learning. *Behavioural Brain Research* 139(1-2), 197-213. doi: 10.1016/s0166-4328(02)00268-1.

Bannerman, D.M., Sprengel, R., Sanderson, D.J., McHugh, S.B., Rawlins, J.N., Monyer, H., et al. (2014). Hippocampal synaptic plasticity, spatial memory and anxiety. *Nat Rev Neurosci* 15(3), 181-192. doi: 10.1038/nrn3677.

Bast, T., Wilson, I.A., Witter, M.P., and Morris, R.G. (2009). From rapid place learning to behavioral performance: a key role for the intermediate hippocampus. *PLoS Biol* 7(4), e1000089. doi: 10.1371/journal.pbio.1000089.

Baumgart, J., and Grebe, N. (2015). C57BL/6-specific conditions for efficient in utero electroporation of the central nervous system. *J Neurosci Methods* 240, 116-124. doi: 10.1016/j.jneumeth.2014.11.004.

Ben-Ari, Y., Cherubini, E., Corradetti, R., and Gaiarsa, J.L. (1989). Giant synaptic potentials in immature rat CA3 hippocampal neurones. *J Physiol* 416, 303-325.

Benchenane, K., Peyrache, A., Khamassi, M., Tierney, P.L., Gioanni, Y., Battaglia, F.P., et al. (2010). Coherent theta oscillations and reorganization of spike timing in the hippocampal- prefrontal network upon learning. *Neuron* 66(6), 921-936. doi: 10.1016/j.neuron.2010.05.013.

Berndt, A., Schoenenberger, P., Mattis, J., Tye, K.M., Deisseroth, K., Hegemann, P., et al. (2011). High-efficiency channelrhodopsins for fast neuronal stimulation at low light levels. *Proc Natl Acad Sci U S A* 108(18), 7595-7600. doi: 10.1073/pnas.1017210108.

Bitzenhofer, S.H., Ahlbeck, J., and Hanganu-Opatz, I.L. (2017a). Methodological Approach for Optogenetic Manipulation of Neonatal Neuronal Networks. *Frontiers in Cellular Neuroscience* 11, 239-252. doi: 10.3389/fncel.2017.00239.

Bitzenhofer, S.H., Ahlbeck, J., Wolff, A., Wiegert, J.S., Gee, C.E., Oertner, T.G., et al. (2017b). Layer-specific optogenetic activation of pyramidal neurons causes beta-gamma entrainment of neonatal networks. *Nat Commun* 8, 14563. doi: 10.1038/ncomms14563.

Bitzenhofer, S.H., and Hanganu-Opatz, I.L. (2014). Oscillatory coupling within neonatal prefrontal-hippocampal networks is independent of selective removal of GABAergic neurons in the hippocampus. *Neuropharmacology* 77, 57-67. doi: 10.1016/j.neuropharm.2013.09.007.

Bitzenhofer, S.H., Sieben, K., Siebert, K.D., Spehr, M., and Hanganu-Opatz, I.L. (2015). Oscillatory activity in developing prefrontal networks results from theta-gamma-modulated synaptic inputs. *Cell Rep* 11(3), 486-497. doi: 10.1016/j.celrep.2015.03.031.

Borrell, V., Yoshimura, Y., and Callaway, E.M. (2005). Targeted gene delivery to telencephalic inhibitory neurons by directional in utero electroporation. *J Neurosci Methods* 143(2), 151-158. doi: 10.1016/j.jneumeth.2004.09.027.

Brincat, S.L., and Miller, E.K. (2015). Frequency-specific hippocampal-prefrontal interactions during associative learning. *Nat Neurosci* 18(4)**,** 576-581. doi: 10.1038/nn.3954.

Brockmann, M.D., Poschel, B., Cichon, N., and Hanganu-Opatz, I.L. (2011). Coupled oscillations mediate directed interactions between prefrontal cortex and hippocampus of the neonatal rat. *Neuron* 71(2)**,** 332-347. doi: 10.1016/j.neuron.2011.05.041.

Buhl, D.L., and Buzsaki, G. (2005). Developmental emergence of hippocampal fast-field "ripple" oscillations in the behaving rat pups. *Neuroscience* 134(4)**,** 1423-1430. doi: 10.1016/j.neuroscience.2005.05.030.

Buzsaki, G. (2015). Hippocampal sharp wave-ripple: A cognitive biomarker for episodic memory and planning. *Hippocampus* 25(10)**,** 1073-1188. doi: 10.1002/hipo.22488.

Cichon, N.B., Denker, M., Grun, S., and Hanganu-Opatz, I.L. (2014). Unsupervised classification of neocortical activity patterns in neonatal and pre-juvenile rodents. *Front Neural Circuits* 8**,** 50. doi: 10.3389/fncir.2014.00050.

Cirelli, C., and Tononi, G. (2015). Cortical development, electroencephalogram rhythms, and the sleep/wake cycle. *Biol Psychiatry* 77(12)**,** 1071-1078. doi: 10.1016/j.biopsych.2014.12.017.

Colgin, L.L. (2011). Oscillations and hippocampal-prefrontal synchrony. *Curr Opin Neurobiol* 21(3)**,** 467-474. doi: 10.1016/j.conb.2011.04.006.

Colgin, L.L. (2016). Rhythms of the hippocampal network. *Nat Rev Neurosci* 17(4)**,** 239-249. doi: 10.1038/nrn.2016.21.

Dong, H.W., Swanson, L.W., Chen, L., Fanselow, M.S., and Toga, A.W. (2009). Genomic-anatomic evidence for distinct functional domains in hippocampal field CA1. *Proc Natl Acad Sci U S A* 106(28)**,** 11794-11799. doi: 10.1073/pnas.0812608106.

Dupont, E., Hanganu, I.L., Kilb, W., Hirsch, S., and Luhmann, H.J. (2006). Rapid developmental switch in the mechanisms driving early cortical columnar networks. *Nature* 439(7072)**,** 79-83. doi: 10.1038/nature04264.

Eichenbaum, H. (2017). Prefrontal-hippocampal interactions in episodic memory. *Nat Rev Neurosci* 18(9)**,** 547-558. doi: 10.1038/nrn.2017.74.

Fanselow, M.S., and Dong, H.W. (2010). Are the dorsal and ventral hippocampus functionally distinct structures? *Neuron* 65(1)**,** 7-19. doi: 10.1016/j.neuron.2009.11.031.

Geisler, C., Robbe, D., Zugaro, M., Sirota, A., and Buzsaki, G. (2007). Hippocampal place cell assemblies are speed-controlled oscillators. *Proc Natl Acad Sci U S A* 104(19)**,** 8149-8154. doi: 10.1073/pnas.0610121104.

Granger, C.W.J. (1980). Testing for causality. *Journal of Economic Dynamics and Control* 2**,** 329-352. doi: 10.1016/0165-1889(80)90069-x.

Hallock, H.L., Wang, A., and Griffin, A.L. (2016). Ventral Midline Thalamus Is Critical for Hippocampal-Prefrontal Synchrony and Spatial Working Memory. *J Neurosci* 36(32)**,** 8372-8389. doi: 10.1523/JNEUROSCI.0991-16.2016.

Hanganu-Opatz, I.L. (2010). Between molecules and experience: role of early patterns of coordinated activity for the development of cortical maps and sensory abilities. *Brain Res Rev* 64(1)**,** 160-176. doi: 10.1016/j.brainresrev.2010.03.005.

Hanganu, I.L., Ben-Ari, Y., and Khazipov, R. (2006). Retinal waves trigger spindle bursts in the neonatal rat visual cortex. *J Neurosci* 26(25)**,** 6728-6736. doi: 10.1523/JNEUROSCI.0752-06.2006.

Hartung, H., Brockmann, M.D., Poschel, B., De Feo, V., and Hanganu-Opatz, I.L. (2016). Thalamic and Entorhinal Network Activity Differently Modulates the Functional Development of Prefrontal-Hippocampal Interactions. *Journal of Neuroscience* 36(13)**,** 3676-3690. doi: 10.1523/jneurosci.3232-15.2016.

Hoerder-Suabedissen, A., and Molnar, Z. (2015). Development, evolution and pathology of neocortical subplate neurons. *Nat Rev Neurosci* 16(3)**,** 133-146. doi: 10.1038/nrn3915.

Honeycutt, J.A., Keary Iii, K.M., Kania, V.M., and Chrobak, J.J. (2016). Developmental Age Differentially Mediates the Calcium-Binding Protein Parvalbumin in the Rat: Evidence for a Selective Decrease in Hippocampal Parvalbumin Cell Counts. *Dev Neurosci* 38(2)**,** 105-114. doi: 10.1159/000444447.

792 Hubel, D.H., Wiesel, T.N., and LeVay, S. (1977). Plasticity of Ocular Dominance Columns in
793 Monkey Striate Cortex. *Philosophical Transactions of the Royal Society B: Biological*
794 *Sciences* 278(961)**,** 377-409. doi: 10.1098/rstb.1977.0050.
795 Huberman, A.D., Speer, C.M., and Chapman, B. (2006). Spontaneous retinal activity
796 mediates development of ocular dominance columns and binocular receptive fields in
797 v1. *Neuron* 52(2)**,** 247-254. doi: 10.1016/j.neuron.2006.07.028.
798 Jay, T.M., and Witter, M.P. (1991). Distribution of hippocampal CA1 and subicular efferents
799 in the prefrontal cortex of the rat studied by means of anterograde transport of
800 Phaseolus vulgaris-leucoagglutinin. *J Comp Neurol* 313(4)**,** 574-586. doi:
801 10.1002/cne.903130404.
802 Khazipov, R., Minlebaev, M., and Valeeva, G. (2013). Early gamma oscillations.
803 *Neuroscience* 250**,** 240-252. doi: 10.1016/j.neuroscience.2013.07.019.
804 Kruger, H.S., Brockmann, M.D., Salamon, J., Ittrich, H., and Hanganu-Opatz, I.L. (2012).
805 Neonatal hippocampal lesion alters the functional maturation of the prefrontal cortex
806 and the early cognitive development in pre-juvenile rats. *Neurobiol Learn Mem* 97(4)**,**
807 470-481. doi: 10.1016/j.nlm.2012.04.001.
808 Lindemann, C., Ahlbeck, J., Bitzenhofer, S.H., and Hanganu-Opatz, I.L. (2016). Spindle
809 Activity Orchestrates Plasticity during Development and Sleep. *Neural Plast* 2016**,**
810 5787423. doi: 10.1155/2016/5787423.
811 Luhmann, H.J., and Khazipov, R. (2017). Neuronal activity patterns in the developing barrel
812 cortex. *Neuroscience*. doi: 10.1016/j.neuroscience.2017.05.025.
813 Minlebaev, M., Ben-Ari, Y., and Khazipov, R. (2009). NMDA receptors pattern early activity in
814 the developing barrel cortex in vivo. *Cereb Cortex* 19(3)**,** 688-696. doi:
815 10.1093/cercor/bhn115.
816 Minlebaev, M., Colonnese, M., Tsintsadze, T., Sirota, A., and Khazipov, R. (2011). Early
817 gamma oscillations synchronize developing thalamus and cortex. *Science* 334(6053)**,**
818 226-229. doi: 10.1126/science.1210574.
819 Moser, E.I. (1998). Impaired Spatial Learning after Saturation of Long-Term Potentiation.
820 *Science* 281(5385)**,** 2038-2042. doi: 10.1126/science.281.5385.2038.
821 Moser, M.B., Moser, E.I., Forrest, E., Andersen, P., and Morris, R.G. (1995). Spatial learning
822 with a minislab in the dorsal hippocampus. *Proc Natl Acad Sci USA* 92(21)**,** 9697-
823 9701.
824 Niwa, M., Kamiya, A., Murai, R., Kubo, K., Gruber, A.J., Tomita, K., et al. (2010). Knockdown
825 of DISC1 by in utero gene transfer disturbs postnatal dopaminergic maturation in the
826 frontal cortex and leads to adult behavioral deficits. *Neuron* 65(4)**,** 480-489. doi:
827 10.1016/j.neuron.2010.01.019.
828 Nolte, G., Bai, O., Wheaton, L., Mari, Z., Vorbach, S., and Hallett, M. (2004). Identifying true
829 brain interaction from EEG data using the imaginary part of coherency. *Clin*
830 *Neurophysiol* 115(10)**,** 2292-2307. doi: 10.1016/j.clinph.2004.04.029.
831 O'Keefe, J., and Nadel, L. (1978). *The Hippocampus as a Cognitive Map.* New York: Oxford
832 University Press.
833 O'Keefe, J., and Recce, M.L. (1993). Phase relationship between hippocampal place units
834 and the EEG theta rhythm. *Hippocampus* 3(3)**,** 317-330. doi:
835 10.1002/hipo.450030307.
836 Patel, J., Schomburg, E.W., Berenyi, A., Fujisawa, S., and Buzsaki, G. (2013). Local
837 generation and propagation of ripples along the septotemporal axis of the
838 hippocampus. *J Neurosci* 33(43)**,** 17029-17041. doi: 10.1523/JNEUROSCI.2036-
839 13.2013.
840 Pitkanen, A., Pikkarainen, M., Nurminen, N., and Ylinen, A. (2000). Reciprocal connections
841 between the amygdala and the hippocampal formation, perirhinal cortex, and
842 postrhinal cortex in rat - A review. *Parahippocampal Region* 911(1)**,** 369-391. doi:
843 10.1111/j.1749-6632.2000.tb06738.x.
844 Place, R., Farovik, A., Brockmann, M., and Eichenbaum, H. (2016). Bidirectional prefrontal-
845 hippocampal interactions support context-guided memory. *Nat Neurosci* 19(8)**,** 992-
846 994. doi: 10.1038/nn.4327.

Rodrigues, P.L., and Baccala, L.A. (2016). Statistically significant time-varying neural connectivity estimation using generalized partial directed coherence. *Conf Proc IEEE Eng Med Biol Soc* 2016**,** 5493-5496. doi: 10.1109/EMBC.2016.7591970.

Royer, S., Sirota, A., Patel, J., and Buzsaki, G. (2010). Distinct representations and theta dynamics in dorsal and ventral hippocampus. *J Neurosci* 30(5)**,** 1777-1787. doi: 10.1523/JNEUROSCI.4681-09.2010.

Seelke, A.M., and Blumberg, M.S. (2010). Developmental appearance and disappearance of cortical events and oscillations in infant rats. *Brain Res* 1324**,** 34-42. doi: 10.1016/j.brainres.2010.01.088.

Shen, J., and Colonnese, M.T. (2016). Development of Activity in the Mouse Visual Cortex. *J Neurosci* 36(48)**,** 12259-12275. doi: 10.1523/JNEUROSCI.1903-16.2016.

Siapas, A.G., Lubenov, E.V., and Wilson, M.A. (2005). Prefrontal phase locking to hippocampal theta oscillations. *Neuron* 46(1)**,** 141-151. doi: 10.1016/j.neuron.2005.02.028.

Siapas, A.G., and Wilson, M.A. (1998). Coordinated interactions between hippocampal ripples and cortical spindles during slow-wave sleep. *Neuron* 21(5)**,** 1123-1128. doi: Doi 10.1016/S0896-6273(00)80629-7.

Sigurdsson, T., Stark, K.L., Karayiorgou, M., Gogos, J.A., and Gordon, J.A. (2010). Impaired hippocampal-prefrontal synchrony in a genetic mouse model of schizophrenia. *Nature* 464(7289)**,** 763-767. doi: 10.1038/nature08855.

Sirota, A., Montgomery, S., Fujisawa, S., Isomura, Y., Zugaro, M., and Buzsaki, G. (2008). Entrainment of neocortical neurons and gamma oscillations by the hippocampal theta rhythm. *Neuron* 60(4)**,** 683-697. doi: 10.1016/j.neuron.2008.09.014.

Spellman, T., Rigotti, M., Ahmari, S.E., Fusi, S., Gogos, J.A., and Gordon, J.A. (2015). Hippocampal-prefrontal input supports spatial encoding in working memory. *Nature* 522(7556)**,** 309-314. doi: 10.1038/nature14445.

Stewart, M., and Fox, S.E. (1990). Do septal neurons pace the hippocampal theta rhythm? *Trends in Neurosciences* 13(5)**,** 163-169. doi: 10.1016/0166-2236(90)90040-h.

Strange, B.A., Witter, M.P., Lein, E.S., and Moser, E.I. (2014). Functional organization of the hippocampal longitudinal axis. *Nat Rev Neurosci* 15(10)**,** 655-669. doi: 10.1038/nrn3785.

Stujenske, J.M., Spellman, T., and Gordon, J.A. (2015). Modeling the Spatiotemporal Dynamics of Light and Heat Propagation for In Vivo Optogenetics. *Cell Rep* 12(3)**,** 525-534. doi: 10.1016/j.celrep.2015.06.036.

Swanson, L.W. (1981). A direct projection from Ammon's horn to prefrontal cortex in the rat. *Brain Res* 217(1)**,** 150-154.

Szczurkowska, J., Cwetsch, A.W., dal Maschio, M., Ghezzi, D., Ratto, G.M., and Cancedda, L. (2016). Targeted in vivo genetic manipulation of the mouse or rat brain by in utero electroporation with a triple-electrode probe. *Nat Protoc* 11(3)**,** 399-412. doi: 10.1038/nprot.2016.014.

Tabata, H., and Nakajima, K. (2001). Efficient in utero gene transfer system to the developing mouse brain using electroporation: Visualization of neuronal migration in the developing cortex. *Neuroscience* 103(4)**,** 865-872. doi: Doi 10.1016/S0306-4522(01)00016-1.

Taxidis, J., Coomber, B., Mason, R., and Owen, M. (2010). Assessing cortico-hippocampal functional connectivity under anesthesia and kainic acid using generalized partial directed coherence. *Biol Cybern* 102(4)**,** 327-340. doi: 10.1007/s00422-010-0370-1.

Thompson, C.L., Pathak, S.D., Jeromin, A., Ng, L.L., MacPherson, C.R., Mortrud, M.T., et al. (2008). Genomic anatomy of the hippocampus. *Neuron* 60(6)**,** 1010-1021. doi: 10.1016/j.neuron.2008.12.008.

Tolner, E.A., Sheikh, A., Yukin, A.Y., Kaila, K., and Kanold, P.O. (2012). Subplate neurons promote spindle bursts and thalamocortical patterning in the neonatal rat somatosensory cortex. *J Neurosci* 32(2)**,** 692-702. doi: 10.1523/JNEUROSCI.1538-11.2012.

Vertes, R.P., Hoover, W.B., Szigeti-Buck, K., and Leranth, C. (2007). Nucleus reuniens of the midline thalamus: link between the medial prefrontal cortex and the hippocampus. *Brain Res Bull* 71(6)**,** 601-609. doi: 10.1016/j.brainresbull.2006.12.002.

Wirt, R.A., and Hyman, J.M. (2017). Integrating Spatial Working Memory and Remote Memory: Interactions between the Medial Prefrontal Cortex and Hippocampus. *Brain Sci* 7(4)**,** 43. doi: 10.3390/brainsci7040043.

Witter, M.P., and Amaral, D.G. (2004). "Hippocampal Formation," in *The Rat Nervous System*. Elsevier Inc.), 635-704.

Witter, M.P., Van Hoesen, G.W., and Amaral, D.G. (1989). Topographical organization of the entorhinal projection to the dentate gyrus of the monkey. *J Neurosci* 9(1)**,** 216-228.

Xu, H.P., Furman, M., Mineur, Y.S., Chen, H., King, S.L., Zenisek, D., et al. (2011). An instructive role for patterned spontaneous retinal activity in mouse visual map development. *Neuron* 70(6)**,** 1115-1127. doi: 10.1016/j.neuron.2011.04.028.

Xu, W., and Sudhof, T.C. (2013). A neural circuit for memory specificity and generalization. *Science* 339(6125)**,** 1290-1295. doi: 10.1126/science.1229534.

Yasuda, M., Johnson-Venkatesh, E.M., Zhang, H., Parent, J.M., Sutton, M.A., and Umemori, H. (2011). Multiple forms of activity-dependent competition refine hippocampal circuits in vivo. *Neuron* 70(6)**,** 1128-1142. doi: 10.1016/j.neuron.2011.04.027.

Ye, X., Kapeller-Libermann, D., Travaglia, A., Inda, M.C., and Alberini, C.M. (2017). Direct dorsal hippocampal-prelimbic cortex connections strengthen fear memories. *Nat Neurosci* 20(1)**,** 52-61. doi: 10.1038/nn.4443.

Yuste, R., Nelson, D.A., Rubin, W.W., and Katz, L.C. (1995). Neuronal domains in developing neocortex: mechanisms of coactivation. *Neuron* 14(1)**,** 7-17.

Zhang, L., Spigelman, I., and Carlen, P.L. (1990). Whole-cell patch study of GABAergic inhibition in CA1 neurons of immature rat hippocampal slices. *Developmental Brain Research* 56(1)**,** 127-130. doi: 10.1016/0165-3806(90)90171-t.

Figure legends

Figure 1. Patterns of discontinuous oscillatory activity in the CA1 area of the neonatal dHP and i/vHP *in vivo*. **(A)** Characteristic theta burst activity recorded in the CA1 area of the dHP (left) and i/vHP (right) of a P9 mouse displayed after band-pass filtering (4-100 Hz) and the corresponding MUA (500-5000 Hz). Color-coded frequency plots show the wavelet spectrum of LFP at identical time scale. **(B)** Bar diagram (mean ± SEM) displaying the occurrence of discontinuous theta bursts in dHP (n=41 mice) and i/vHP (n=103 mice). **(C)** Power analysis of discontinuous oscillatory activity P(f) normalized to the non-oscillatory period $P_0(f)$ in dHP and i/vHP. (i) Power spectra (4-100 Hz) averaged for all investigated mice. (ii) Bar diagrams quantifying the mean power within theta frequency band (4-12 Hz) in dHP (n=41 mice) and i/vHP (n=103 mice) **(D)** Bar diagram displaying the SUA of dHP (n=158 units) and i/vHP (n=557 units) after clustering of spike shapes. **(E)** Characteristic SPWs and ripple events recorded in dHP (left) and i/vHP (right). **(F)** Bar diagrams (mean ± SEM) displaying the SPWs occurrence in dHP and i/vHP. **(G)** Characteristic SPW-ripple events recorded in dHP (left) and i/vHP (right). **(H)** Bar diagram displaying the mean power of ripples in dHP and i/vHP. **(I)** Spike trains from neurons in dHP (left) and i/vHP (right) aligned to SPWs. **(J)** Histograms of SUA aligned to SPWs (n=232 units for dHP, n=670 for i/vHP). Data are represented as mean ± SEM. *p < 0.05, **p < 0.01, ***p < 0.001.

Figure 2. Dynamic coupling of hippocampal and prefrontal oscillatory activity along septo-temporal axis during neonatal development. **(A)** Simultaneous LFP recordings of discontinuous oscillatory activity in dHP and PL (top) and i/vHP and PL (bottom). **(B)** Long-range synchrony within prefrontal-hippocampal networks. (i) Average coherence spectra for simultaneously recorded oscillatory events in dHP and PL as well as i/vHP and PL. (ii) Bar diagrams (mean ± SEM) displaying the coherence in theta (4-12 Hz), beta (12-30 Hz), and gamma (30-100 Hz) band when averaged for all investigated mice. **(C)** Directed interactions between PL and either dHP or i/vHP monitored by general Partial Directed Coherence (gPDC). Bar diagrams displaying the gPDC calculated for theta (4-12 Hz, left) and beta (12-

30 Hz, right) frequency and averaged for all investigated animals (n=41 mice for dHP and PL, n=103 mice for i/vHP & PL). **(D)** Histograms displaying the phase-locking of prelimbic spikes to theta oscillations in dHP (left) and i/vHP (right). Note the different proportion of spikes significantly locked along the septo-temporal axis (dHP, 3 of 46 units; i/vHP, 52 of 310 units). Data are represented as mean ± SEM. *p < 0.05, ***p < 0.001.

Figure 3. Coupling between neonatal PFC and HP during hippocampal SPWs**. (A)** Power changes in the PL during hippocampal SPWs. (i) Color-coded frequency plot showing the relative power in the PL aligned to the onset of SPWs detected in i/vHP when normalized to the power change caused in the PL by SPWs in the dHP. All other colors than green represent power augmentation (red) or decrease (blue). (ii) Bar diagrams displaying mean power changes of prelimbic activity in different frequency bands (left, theta; middle, beta; right, gamma) before (pre) and after (post) hippocampal SPWs in the dHP and i/vHP (n=41 mice for dHP, n=103 mice for i/vHP). **(B)** Spike trains recorded in the PL before and after SPWs occurring either in the dHP (left) or i/vHP (right). **(C)** Histograms of prelimbic spiking in relationship with hippocampal SPWs (n=148 units for dHP, n=560 units for i/vHP). Data are represented as mean ± SEM. *p < 0.05, **p < 0.01, ***p < 0.001.

Figure 4. Long-range monosynaptic axonal projections connecting the neonatal PFC and hippocampal CA1 area along the septo-temporal axis. **(A)** Photomicrographs depicting dense retrogradely labelled neurons in the CA1 area of i/vHP (right) but not dHP (middle) after FG injection into PL at P1 (left). Bar diagram displays the overall density of retrogradely stained neurons when averaged for all investigated pups (n=8 mice). **(B)** Photomicrographs depicting anterogradely labeled axons targeting the PL of a P10 mouse (right) after iontophoretic BDA injection into the CA1 area of i/vHP at P7 (left). The site of injection and the area with the highest axonal density are depicted at higher magnification. Data are represented as mean ± SEM. ***p < 0.001.

Figure 5. Optogenetic activation of pyramidal neurons in the CA1 area of dHP and i/vHP has different effects on the network activity of neonatal PL. **(A)** Cell- and layer-specific transfection of dHP or i/vHP with CAG-ChR2(ET/TC)-2A-tDimer2 by site-directed IUE. (i) Photomicrographs depicting tDimer2-expressing pyramidal neurons (red) in the CA1 region of dHP (left) and i/vHP (right) when stained for NeuN (green, top panels) or GABA (green, bottom panels). (ii) Photomicrographs depicting the transfected hippocampal neurons when co-stained for NeuN and displayed at larger magnification. (iii) Photomicrographs depicting transfected hippocampal neurons when co-stained for GABA and displayed at larger magnification. **(B)** Optogenetic activation of pyramidal neurons in CA1 area along septo-temporal axis. (i) Representative raster plot and corresponding spike probability histogram for dHP (left) and i/vHP (right) in response to 30 sweeps of 8 Hz pulse stimulation (3 ms pulse length, 473 nm). (ii) Bar diagram displaying the efficacy of inducing spiking in dHP and i/vHP of different stimulation frequencies. **(C)** Characteristic light-induced discontinuous oscillatory activity in the PL of a P10 mouse after transfection of pyramidal neurons in the CA1 area of the dHP (left) or i/vHP (right) with ChR2(ET/TC) by IUE. The LFP is displayed after band-pass filtering (4-100 Hz) together with the corresponding color-coded wavelet spectrum at identical time scale. **(D)** Power analysis of prelimbic oscillatory activity $P_{stim}(f)$ after light stimulation of dHP (green) and i/v HP (orange) at different frequencies (4, 8, 16 Hz) normalized to the activity before stimulus $P_{pre}(f)$. (i) Power spectra (0-100 Hz) averaged for all investigated mice. (ii) Bar diagrams displaying mean power changes in PL during stimulation of either dHP (top panels) or i/vHP (bottom panels). Data are represented as mean ± SEM. *p < 0.05, **p < 0.01.

Table legends

Table 1.

Mean power changes in PL after light stimulation of dHP or i/vHP in ChR2(ET/TC)-containing and opsin-free animals. *p < 0.05, **p < 0.01.

Supplementary figure legends

Figure S1 (Figure Supplement 1 for Figure 1). Properties of network and neuronal activity in i/vHP of neonatal non-anesthetized and urethane-anesthetized mice. **(A)** Plots displaying the mean power of oscillatory events for theta, beta and gamma frequencies before and after urethane anesthesia (n=9 mice). **(B)** Same as (A) for mean coherence between oscillatory events in i/vHP and PL. **(C)** Same as (A) for directed interactions between i/vHP and PL measured by mean gPDC in theta and beta frequency bands. **(D)** Impact of urethane anesthesia on the firing rate (i) and phase locking to theta, beta, and gamma oscillatory network activity. Each line corresponds to one investigated pup. Error bars represent SEM. *p < 0.05, **p <0.01.

Figure S2 (Figure supplement 2 for Figure 1). Properties of network and neuronal activity in dHP vs. i/vHP of neonatal mice. **(A)** Bar diagrams displaying the amplitude and duration of discontinuous oscillatory events in dHP (n=41 mice) and i/vHP (n=103 mice). **(B)** Bar diagrams displaying the power spectrum of discontinuous oscillatory activity P(f) normalized to the non-oscillatory period P0(f) when averaged for beta (12-30 Hz) and gamma (30-100 Hz) frequency bands in dHP (left, n=41 mice) and i/vHP (right, n=103 mice). **(C)** Histograms displaying the phase-locking of hippocampal spikes to ripple activity in dHP (left) and i/vHP (right). Error bars represent SEM. **p < 0.01, ***p < 0.001.

Figure S3 (Figure supplement 1 for figure 5). Experimental protocol for in utero electroporation of the hippocampus. **(A)** Structure of the ChR2(ET/TC)-containing and opsin-free constructs. **(B)** Schematic drawing illustrating the orientation of electrode paddles for specific targeting of either (i) dHP or (ii) i/vHP pyramidal neurons. **(C)** Bar diagram displaying the mean number of embryos, electroporated embryos, surviving pups, and positively transfected pups when ChR2(ET/TC)-containing and opsin-free constructs for (i) dHP (n=8 litters for opsin-containing group, n=5 for opsin-free group) and (ii) i/vHP (n=8 litters for opsin-containing group, n=3 litters for opsin-free group). **(D)** Line plots displaying the

1041 developmental profile of somatic growth [body length, tail length, weight] and reflexes
1042 [vibrissa placing, cliff aversion and surface righting reflexes] of P2-8 pups expressing
1043 ChR2(ET/TC) or opsin-free constructs in (i) dHP (n=17 for opsin-containing pups, n=14 for
1044 opsin-free pups) and (ii) i/vHP (n=9 for opsin-containing pups, n=5 for opsin-free pups). Error
1045 bars represent SEM.
1046
1047 **Figure S4 (Figure supplement 2 for figure 5).** Response in prelimbic cortex for opsin-free
1048 animals. Bar diagrams displaying the power changes in PL during light stimulation of
1049 pyramidal neurons in the CA1 area of dHP (top panels) or i/vHP (bottom panels) when
1050 normalized to the values before hippocampal stimulation for opsin-free animals. Error bars
1051 represent SEM.
1052
1053 **Supplementary table legends**
1054 **Table S1 (table supplement 1 for figures 1-5 & supplementary figures 1-4)** Summary of
1055 statistics for all experiments. (A) Statistical testing, number of investigated mice and p-values
1056 for the analyses displayed in figure 1. (B)–(H) Same as (A) for analyses in figures 2–5, S1-4.

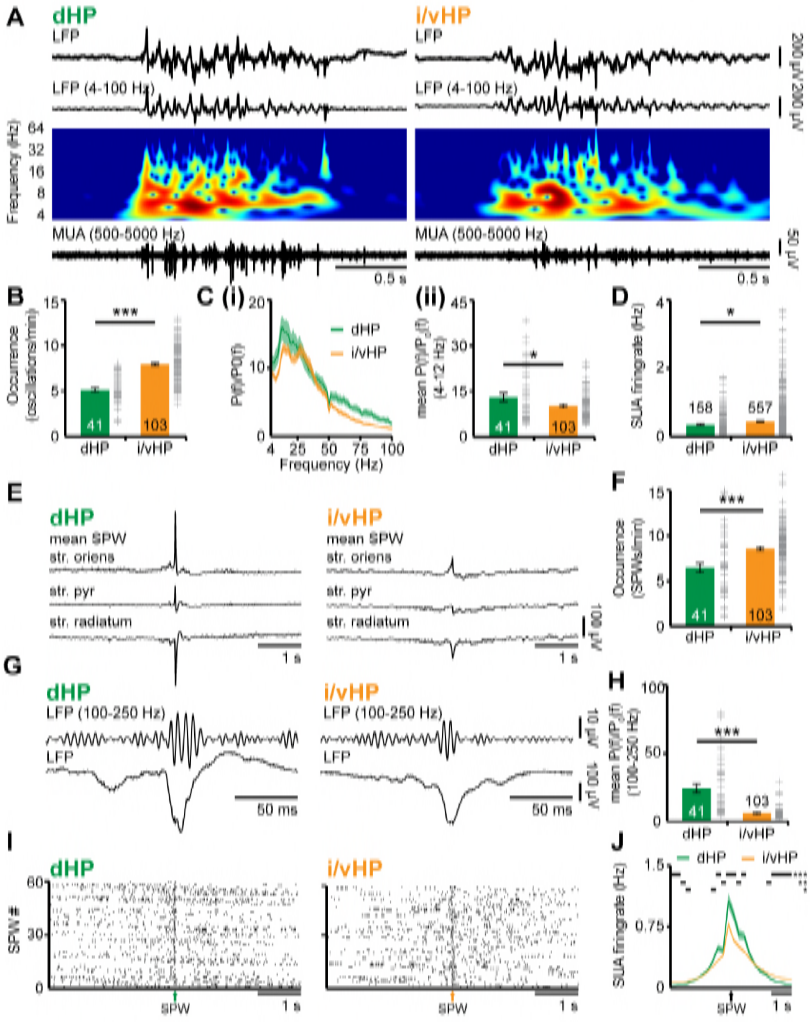

Ahlbeck et al., Figure 1

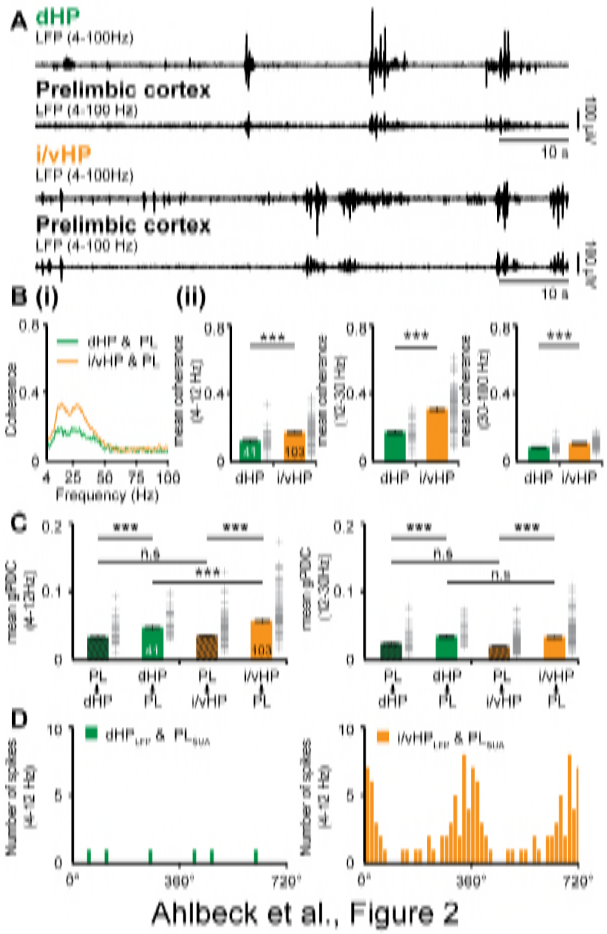

Ahlbeck et al., Figure 2

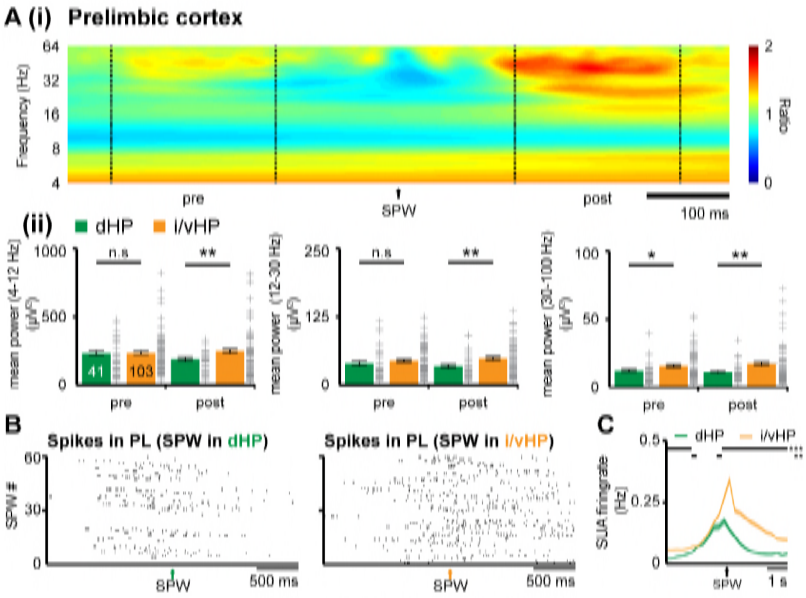

Ahlbeck et al., Figure 3

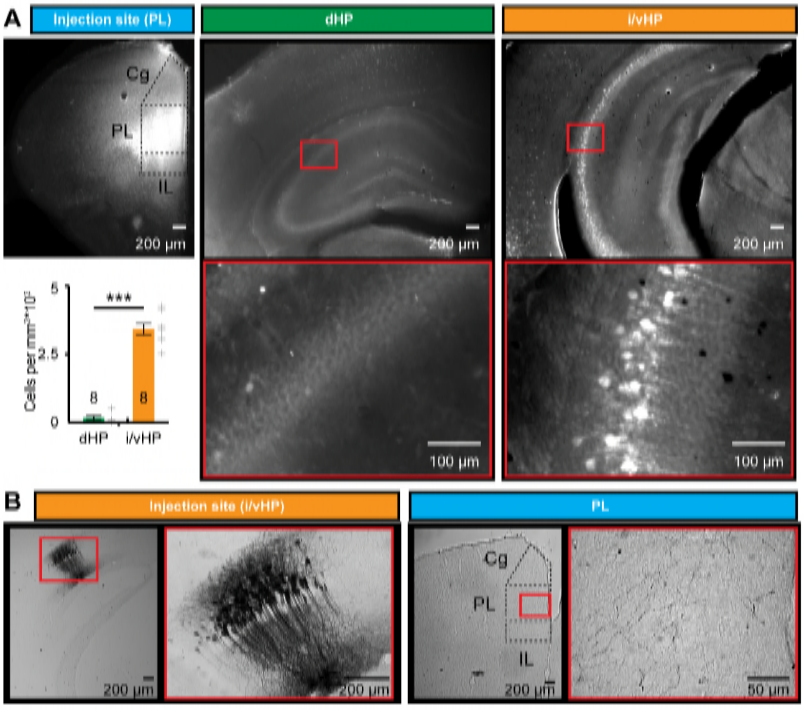

Ahlbeck et al., Figure 4

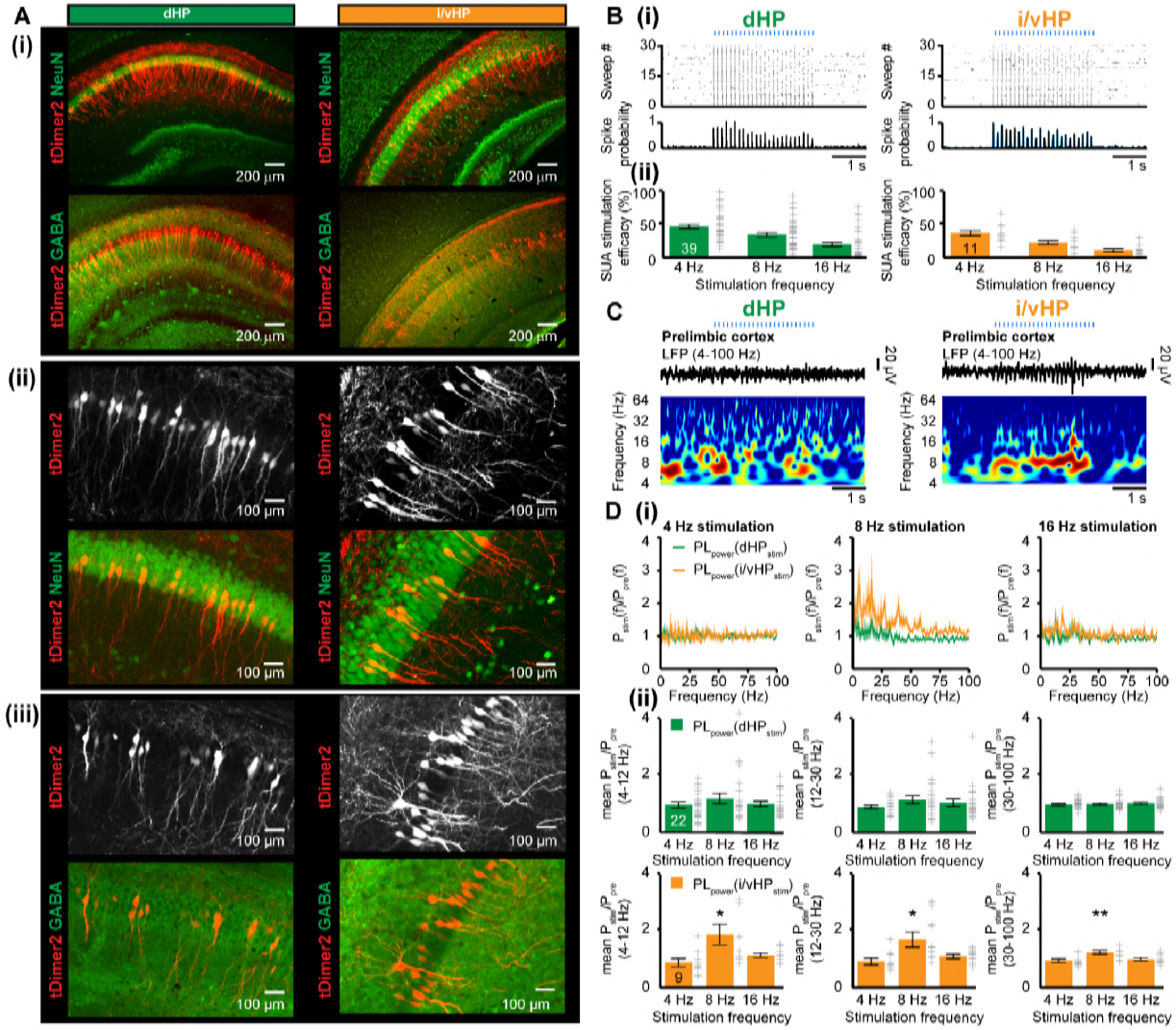

Ahlbeck et al., Figure 5

	dHP			i/vHP		
	Stimulation Frequency			Stimulation Frequency		
ChR2(ET/TC)	**4 Hz**	**8 Hz**	**16 Hz**	**4 Hz**	**8 Hz**	**16hz**
Theta	0.97±0.10	1.19±0.19	1.0±0.093	0.90±0.15	1.89±0.36 (*)	1.16±0.08
Beta	0.91±0.06	1.17±0.15	1.06±0.13	0.94±0.12	1.72±0.27 (*)	1.12±0.08
Gamma	1.0±0.035	1.00±0.19	1.04±0.38	0.97±0.06	1.26±0.06 (**)	1.02±0.06
Opsinfree						
Theta	1.11±0.14	1.09±0.19	1.14±0.22	1.17±0.27	1.17±0.20	1.16±0.12
Beta	1.13±0.15	0.99±0.16	1.11±0.11	1.05±0.22	0.95±0.18	1.08±0.13
Gamma	1.08±0.06	0.93±0.04	1.03±0.03	0.89±0.09	0.94±0.07	0.97±0.04

Table 1

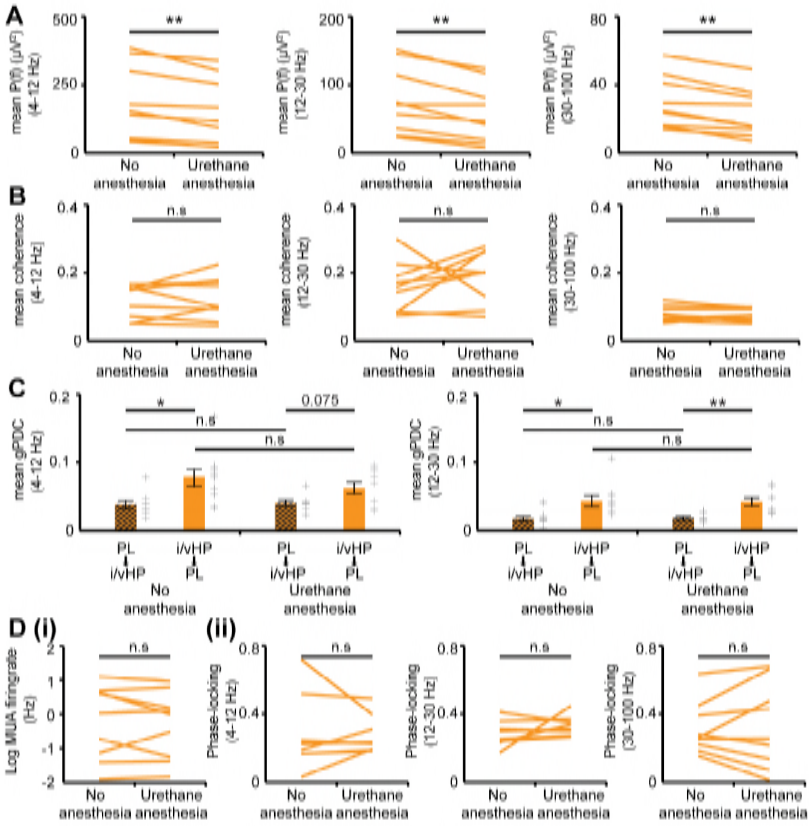

Ahlbeck et al., Figure S1

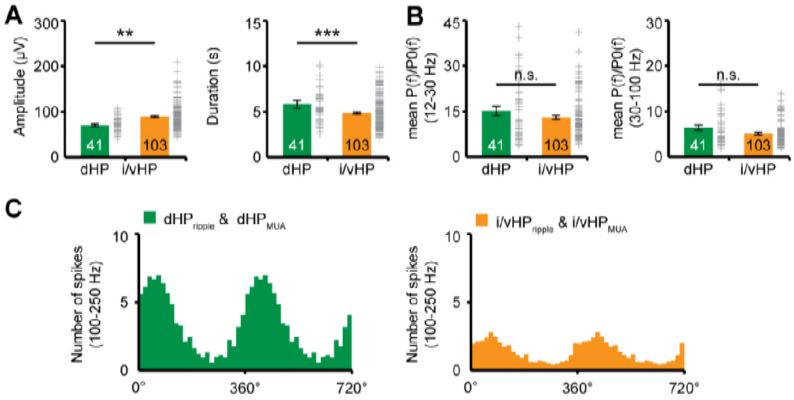

Ahlbeck et al., Figure S2

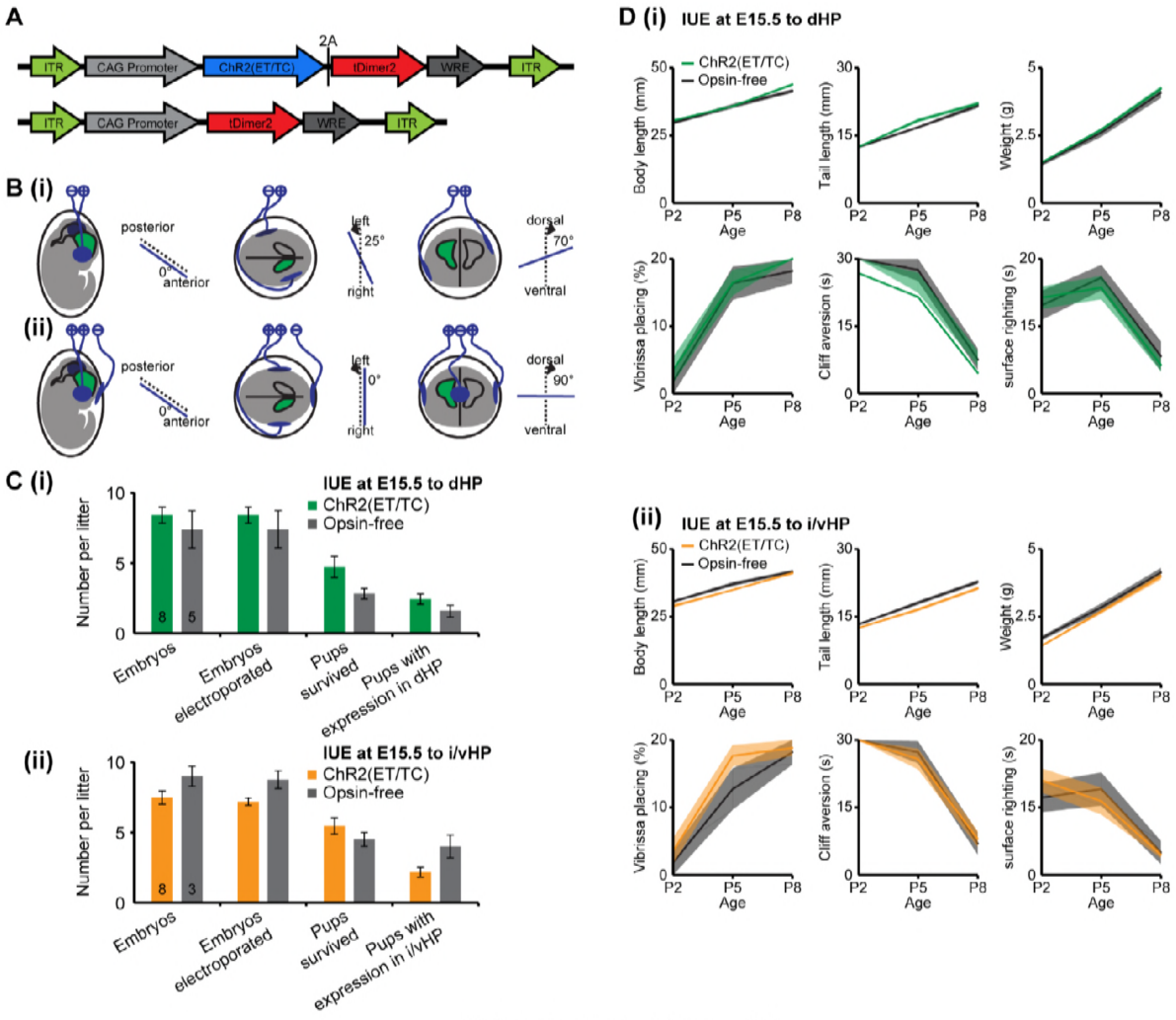

Ahlbeck et al., Figure S3

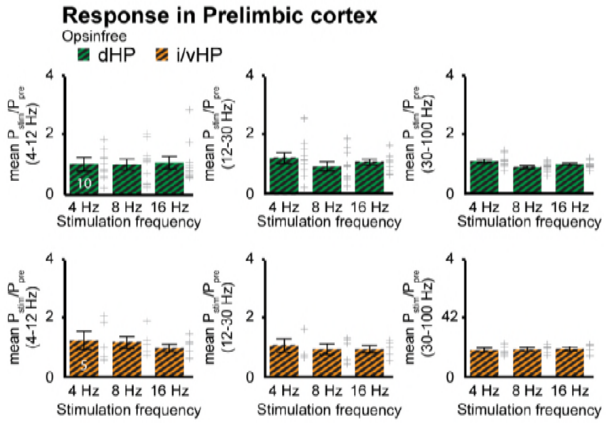

Ahlbeck et al., Figure S4

Supplementary table 1

A

Figure	Panel	Title	Description	Detail	Test	n	p
1	B	Occurrence	Occurrence of theta burst oscillations in hippocampus		t-test	dHP: 41 mice; i/vHP: 103 mice	<0.001
	C(ii)	Power	Theta power in hippocampus		t-test	dHP: 41 mice; i/vHP: 103 mice	0.026
	D	SUA firingrate	SUA firingrate in hippocampus		t-test	dHP: 158 units; i/vHP 557 units	0.025
	F	Occurrence	Occurrenc of sharpwave-ripple complex in hippocampus		t-test	dHP: 41 mice; i/vHP: 103 mice	<0.001
	H	Power	Ripple power in hippocampus		t-test	dHP: 41 mice; i/vHP: 103 mice	<0.001
	J	SUA firingrate	SUA firingrate in hippocampus alighned to sharpwave-ripple complex	0-250 ms	One-way ANOVA – Bonferroni-Holm corrected	dHP: 232 units; i/vHP 670 units	<0.001
				250-500 ms	One-way ANOVA – Bonferroni-Holm corrected	dHP: 232 units; i/vHP 670 units	<0.001
				500-750 ms	One-way ANOVA – Bonferroni-Holm corrected	dHP: 232 units; i/vHP 670 units	0.0022
				750-1000 ms	One-way ANOVA – Bonferroni-Holm corrected	dHP: 232 units; i/vHP 670 units	0.17
				1000-1250 ms	One-way ANOVA – Bonferroni-Holm corrected	dHP: 232 units; i/vHP 670 units	0.28
				1250-1500 ms	One-way ANOVA – Bonferroni-Holm corrected	dHP: 232 units; i/vHP 670 units	0.72
				1500-1750 ms	One-way ANOVA – Bonferroni-Holm corrected	dHP: 232 units; i/vHP 670 units	0.29
				1750-2000 ms	One-way ANOVA – Bonferroni-Holm corrected	dHP: 232 units; i/vHP 670 units	0.42
				2000-2250 ms	One-way ANOVA – Bonferroni-Holm corrected	dHP: 232 units; i/vHP 670 units	0.01
				2250-2500 ms	One-way ANOVA – Bonferroni-Holm corrected	dHP: 232 units; i/vHP 670 units	<0.001
				2500-2750 ms	One-way ANOVA – Bonferroni-Holm corrected	dHP: 232 units; i/vHP 670 units	0.093
				2750-3000 ms	One-way ANOVA – Bonferroni-Holm corrected	dHP: 232 units; i/vHP 670 units	<0.001
				3000-3250 ms	One-way ANOVA – Bonferroni-Holm corrected	dHP: 232 units; i/vHP 670 units	<0.001
				3250-3500 ms	One-way ANOVA – Bonferroni-Holm corrected	dHP: 232 units; i/vHP 670 units	0.0063
				3500-3750 ms	One-way ANOVA – Bonferroni-Holm corrected	dHP: 232 units; i/vHP 670 units	<0.001

				3750-4000 ms	One-way ANOVA – Bonferroni-Holm corrected	dHP: 232 units; i/vHP 670 units	0.083
				4000-4250 ms	One-way ANOVA – Bonferroni-Holm corrected	dHP: 232 units; i/vHP 670 units	0.99
				4250-4500 ms	One-way ANOVA – Bonferroni-Holm corrected	dHP: 232 units; i/vHP 670 units	0.83
				4500-4750 ms	One-way ANOVA – Bonferroni-Holm corrected	dHP: 232 units; i/vHP 670 units	0.27
				4750-5000 ms	One-way ANOVA – Bonferroni-Holm corrected	dHP: 232 units; i/vHP 670 units	0.0021
				5000-5250 ms	One-way ANOVA – Bonferroni-Holm corrected	dHP: 232 units; i/vHP 670 units	<0.001
				5250-5500 ms	One-way ANOVA – Bonferroni-Holm corrected	dHP: 232 units; i/vHP 670 units	<0.001
				5500-5750 ms	One-way ANOVA – Bonferroni-Holm corrected	dHP: 232 units; i/vHP 670 units	<0.001
				5750-6000 ms	One-way ANOVA – Bonferroni-Holm corrected	dHP: 232 units; i/vHP 670 units	<0.001

B

Figure	Panel	Title	Description	Detail	Test	n	p
2	B(ii)	Coherence	Coherence between hippocampus and prefrontal cortex	4-12 Hz	t-test	dHP: 41 mice; i/vHP: 103 mice	<0.001
				12-30 Hz	t-test	dHP: 41 mice; i/vHP: 103 mice	<0.001
				30-100Hz	t-test	dHP: 41 mice; i/vHP: 103 mice	<0.001
	C	gPDC	gPDC between hippocampus and prefrontal cortex	4-12 Hz, PL→dHP & dHP→PL	paired t-test	41 mice	<0.001
				4-12 Hz, PL→i/VHP & i/vHP→PL	paired t-test	103 mice	<0.001
				4-12 Hz, PL→dHP & PL→i/vHP	t-test	dHP: 41 mice; i/vHP: 103 mice	0.065
				4-12 Hz, dHP→PL & i/vHP→PL	t-test	dHP: 41 mice; i/vHP: 103 mice	<0.001
				12-30 Hz, PL→dHP & dHP→PL	paired t-test	41 mice	<0.001

				12-30 Hz, PL→i/VHP & i/vHP→PL	paired t-test	103 mice	<0.001
				12-30 Hz, PL→dHP & PL→i/vHP	t-test	dHP: 41 mice; i/vHP: 103 mice	0.66
				12-30 Hz, dHP→PL & i/vHP→PL	t-test	dHP: 41 mice; i/vHP: 103 mice	0.16

C

Figure	Panel	Title	Description	Detail	Test	n	p
3	A(ii)	Power	Power between hippocampus and prefrontal cortex aligned to sharpwave-ripple complex	4-12 Hz	t-test	dHP: 41 mice; i/vHP: 103 mice	<0.001
				12-30 Hz	t-test	dHP: 41 mice; i/vHP: 103 mice	<0.001
				30-100Hz	t-test	dHP: 41 mice; i/vHP: 103 mice	<0.001
	C	SUA firingrate	SUA firingrate in prefrontal cortex alighned to sharpwave-ripple complex	0-250 ms	One-way ANOVA – Bonferroni-Holm corrected	dHP: 148 units; i/vHP 561 units	<0.001
				250-500 ms	One-way ANOVA – Bonferroni-Holm corrected	dHP: 148 units; i/vHP 561 units	<0.001
				500-750 ms	One-way ANOVA – Bonferroni-Holm corrected	dHP: 148 units; i/vHP 561 units	<0.001
				750-1000 ms	One-way ANOVA – Bonferroni-Holm corrected	dHP: 148 units; i/vHP 561 units	<0.001
				1000-1250 ms	One-way ANOVA – Bonferroni-Holm corrected	dHP: 148 units; i/vHP 561 units	<0.001
				1250-1500 ms	One-way ANOVA – Bonferroni-Holm corrected	dHP: 148 units; i/vHP 561 units	0.0042
				1500-1750 ms	One-way ANOVA – Bonferroni-Holm corrected	dHP: 148 units; i/vHP 561 units	0.96
				1750-2000 ms	One-way ANOVA – Bonferroni-Holm corrected	dHP: 148 units; i/vHP 561 units	0.09
				2000-2250 ms	One-way ANOVA – Bonferroni-Holm corrected	dHP: 148 units; i/vHP 561 units	0.16
				2250-2500 ms	One-way ANOVA – Bonferroni-Holm corrected	dHP: 148 units; i/vHP 561 units	0.39
				2500-2750 ms	One-way ANOVA – Bonferroni-Holm corrected	dHP: 148 units; i/vHP 561 units	0.009
				2750-3000 ms	One-way ANOVA – Bonferroni-Holm corrected	dHP: 148 units; i/vHP 561 units	<0.001

				3000-3250 ms	One-way ANOVA – Bonferroni-Holm corrected	dHP: 148 units; i/vHP 561 units	<0.001
				3250-3500 ms	One-way ANOVA – Bonferroni-Holm corrected	dHP: 148 units; i/vHP 561 units	<0.001
				3500-3750 ms	One-way ANOVA – Bonferroni-Holm corrected	dHP: 148 units; i/vHP 561 units	<0.001
				3750-4000 ms	One-way ANOVA – Bonferroni-Holm corrected	dHP: 148 units; i/vHP 561 units	<0.001
				4000-4250 ms	One-way ANOVA – Bonferroni-Holm corrected	dHP: 148 units; i/vHP 561 units	<0.001
				4250-4500 ms	One-way ANOVA – Bonferroni-Holm corrected	dHP: 148 units; i/vHP 561 units	<0.001
				4500-4750 ms	One-way ANOVA – Bonferroni-Holm corrected	dHP: 148 units; i/vHP 561 units	<0.001
				4750-5000 ms	One-way ANOVA – Bonferroni-Holm corrected	dHP: 148 units; i/vHP 561 units	<0.001
				5000-5250 ms	One-way ANOVA – Bonferroni-Holm corrected	dHP: 148 units; i/vHP 561 units	<0.001
				5250-5500 ms	One-way ANOVA – Bonferroni-Holm corrected	dHP: 148 units; i/vHP 561 units	<0.001
				5500-5750 ms	One-way ANOVA – Bonferroni-Holm corrected	dHP: 148 units; i/vHP 561 units	<0.001
				5750-6000 ms	One-way ANOVA – Bonferroni-Holm corrected	dHP: 148 units; i/vHP 561 units	<0.001

D

Figure	Panel	Title	Description	Detail	Test	n	p
4	A	retrograde tracing	Retrograde labelled neurons in dHP & i/vHP		paired t-test	8 mice	<0.001

E

Figure	Panel	Title	Description	Detail	Test	n	p
5	D(ii)	Power	power response in PL during light stimulation in HP	PL_Power(dHP stimulation); 4-12 Hz, 4 Hz stimulation	One-sample t-test	22 mice	0.76
				PL_Power(dHP stimulation); 4-12 Hz, 8 Hz stimulation	One-sample t-test	22 mice	0.33
				PL_Power(dHP stimulation); 4-12 Hz, 16 Hz stimulation	One-sample t-test	22 mice	0.95

				PL_Power(dHP stimulation); 12-30 Hz, 4 Hz stimulation	One-sample t-test	22 mice	0.17
				PL_Power(dHP stimulation); 12-30 Hz, 8 Hz stimulation	One-sample t-test	22 mice	0.28
				PL_Power(dHP stimulation); 12-30 Hz, 16 Hz stimulation	One-sample t-test	22 mice	0.64
				PL_Power(dHP stimulation); 30-100 Hz, 4 Hz stimulation	One-sample t-test	22 mice	1
				PL_Power(dHP stimulation); 30-100 Hz, 8 Hz stimulation	One-sample t-test	22 mice	0.64
				PL_Power(dHP stimulation); 30-100 Hz, 16 Hz stimulation	One-sample t-test	22 mice	0.28
				PL_Power(i/vHP stimulation); 4-12 Hz, 4 Hz stimulation	One-sample t-test	9 mice	0.51
				PL_Power(i/vHP stimulation); 4-12 Hz, 8 Hz stimulation	One-sample t-test	9 mice	0.039
				PL_Power(i/vHP stimulation); 4-12 Hz, 16 Hz stimulation	One-sample t-test	9 mice	0.096
				PL_Power(i/vHP stimulation); 12-30 Hz, 4 Hz stimulation	One-sample t-test	9 mice	0.61
				PL_Power(i/vHPHP stimulation); 12-30 Hz, 8 Hz stimulation	One-sample t-test	9 mice	0.03

				PL_Power(i/vHPHP stimulation); 12-30 Hz, 16 Hz stimulation	One-sample t-test	9 mice	0.17
				PL_Power(i/vHPHP stimulation); 30-100 Hz, 4 Hz stimulation	One-sample t-test	9 mice	0.58
				PL_Power(i/vHPHP stimulation); 30-100 Hz, 8 Hz stimulation	One-sample t-test	9 mice	0.0036
				PL_Power(i/vHP stimulation); 30-100 Hz, 16 Hz stimulation	One-sample t-test	9 mice	0.80

F

Figure	Panel	Title	Description	Detail	Test	n	p
S1	A	Power	Power in hippocampus with and without anesthesia	4-12 Hz	paired t-test	9 mice	0.0039
				12-30 Hz	paired t-test	9 mice	0.0078
				30-100 Hz	paired t-test	9 mice	0.0039
	B	Coherence	Coherence between hippocampus and prefrontal cortex with and without anesthesia	4-12 Hz	paired t-test	9 mice	0.61
				12-30 Hz	paired t-test	9 mice	0.39
				30-100 Hz	paired t-test	9 mice	0.48
	C	gPDC	gPDC between hippocampus and prefrontal cortex with and without anesthesia	4-12 Hz, No Anesthesia PL→i/vHP & i/vHP→PL	paired t-test	9 mice	0.027
				4-12 Hz, Urethane anesthesia PL→i/VHP & i/vHP→PL	paired t-test	9 mice	0.075
				4-12 Hz, PL→i/vHP anesthesia & urethane anesthesia	paired t-test	9 mice	0.18

				4-12 Hz, i/vHP→PL anesthesia & urethane anesthesia	paired t-test	9 mice	0.78
				12-30 Hz, PL→dHP & dHP→PL	paired t-test	9 mice	0.045
				12-30 Hz, PL→i/VHP & i/vHP→PL	paired t-test	9 mice	0.0088
				12-30 Hz, PL→dHP & PL→i/vHP	paired t-test	9 mice	0.093
				12-30 Hz, dHP→PL & i/vHP→PL	paired t-test	9 mice	0.77
	D(i)	Log MUA firingrate	Firingrate of MUA in hippocampus		paired t-test	9 mice	0.65
	D(ii)	Phase-locking	Phase-locking of hippocampal MUA to local field potential in hippocampus	4-12 Hz	Wilcoxon rank sumtest for equal medians	9 mice	0.16
				12-30 Hz	Wilcoxon rank sumtest for equal medians	9 mice	0.91
				30-100 Hz	Wilcoxon rank sumtest for equal medians	9 mice	1

G

Figure	Panel	Title	Description	Detail	Test	n	p
S2	A	Amplitude	Theta burst amplitude in hippocampus		t-test	dHP: 41 mice; i/vHP: 103 mice	0.015
		Duration	Theta burst duration in hippocampus		t-test	dHP: 41 mice; i/vHP: 103 mice	<0.001
	B	Power	beta power in hippocampus	12-30 Hz	t-test	dHP: 41 mice; i/vHP: 103 mice	0.22
			gamma power in hippocampus	30-100 Hz	t-test	dHP: 41 mice; i/vHP: 103 mice	0.073

H

Figure	Panel	Title	Description	Detail	Test	n	p
S4		Power	power response in PL during light stimulation in HP	PL_Power(dHP stimulation); 4-12 Hz, 4 Hz stimulation	One-sample t-test	10 mice	0.46

				PL_Power(dHP stimulation); 4-12 Hz, 8 Hz stimulation	One-sample t-test	10 mice	0.65
				PL_Power(dHP stimulation); 4-12 Hz, 16 Hz stimulation	One-sample t-test	10 mice	0.55
				PL_Power(dHP stimulation); 12-30 Hz, 4 Hz stimulation	One-sample t-test	10 mice	0.39
				PL_Power(dHP stimulation); 12-30 Hz, 8 Hz stimulation	One-sample t-test	10 mice	0.98
				PL_Power(dHP stimulation); 12-30 Hz, 16 Hz stimulation	One-sample t-test	10 mice	0.32
				PL_Power(dHP stimulation); 30-100 Hz, 4 Hz stimulation	One-sample t-test	10 mice	0.22
				PL_Power(dHP stimulation); 30-100 Hz, 8 Hz stimulation	One-sample t-test	10 mice	0.11
				PL_Power(dHP stimulation); 30-100 Hz, 16 Hz stimulation	One-sample t-test	10 mice	0.46
				PL_Power(i/vHP stimulation); 4-12 Hz, 4 Hz stimulation	One-sample t-test	5 mice	0.46
				PL_Power(i/vHP stimulation); 4-12 Hz, 8 Hz stimulation	One-sample t-test	5 mice	0.35
				PL_Power(i/vHP stimulation); 4-12 Hz, 16 Hz stimulation	One-sample t-test	5 mice	0.24

				PL_Power(i/vHP stimulation); 12-30 Hz, 4 Hz stimulation	One-sample t-test	5 mice	0.74
				PL_Power(i/vHPHP stimulation); 12-30 Hz, 8 Hz stimulation	One-sample t-test	5 mice	0.85
				PL_Power(i/vHPHP stimulation); 12-30 Hz, 16 Hz stimulation	One-sample t-test	5 mice	0.57
				PL_Power(i/vHPHP stimulation); 30-100 Hz, 4 Hz stimulation	One-sample t-test	5 mice	0.35
				PL_Power(i/vHPHP stimulation); 30-100 Hz, 8 Hz stimulation	One-sample t-test	5 mice	0.56
				PL_Power(i/vHP stimulation); 30-100 Hz, 16 Hz stimulation	One-sample t-test	5 mice	0.49